Editors' Suggestion

Quantum many-body states and Green's functions of nonequilibrium electron-magnon systems: Localized spin operators versus their mapping to Holstein-Primakoff bosons

Utkarsh Bajpai,[1,2] Abhin Suresh,[1] and Branislav K. Nikolić[1,*]

[1]*Department of Physics and Astronomy, University of Delaware, Newark, Delaware 19716, USA*

[2]*Department of Physics and Astronomy, Clemson University, Clemson, South Carolina 29634, USA*

(Received 21 July 2021; revised 17 October 2021; accepted 25 October 2021; published 22 November 2021)

It is well-known that operators of localized spins within a magnetic material satisfy neither fermionic nor bosonic commutation relations. Thus, to construct diagrammatic many-body perturbation theory requiring the Wick theorem, the spin operators are usually mapped to the bosonic ones with Holstein-Primakoff (HP) transformation being the most widely used in magnonics and spintronics literature. However, to make calculations tractable, the square root of operators in the HP transformation is expanded into a Taylor series truncated to some low order. This poses a question on the *range of validity of the truncated HP transformation* when describing nonequilibrium dynamics of localized spins interacting with each other or with conduction electron spins—a problem frequently encountered in numerous transport phenomena in magnonics and spintronics. Here we apply exact diagonalization techniques to a Hamiltonian of fermions (i.e., electrons) interacting with HP bosons versus a Hamiltonian of fermions interacting with the original localized spin operators to compare their many-body states and one-particle equilibrium and nonequilibrium Green's functions (GFs). We employ as a test bed a one-dimensional quantum Heisenberg ferromagnetic spin-S XXX chain of $N \leqslant 7$ sites, where $S = 1$ or $S = 5/2$, and the ferromagnet can be made metallic by allowing electrons to hop between the sites while interacting with the localized spins via *sd* exchange interaction. For these two different versions of the Hamiltonian of this model, we compare the structure of their ground states, time evolution of excited states, spectral functions computed from the retarded GF in equilibrium, and matrix elements of the lesser GF out of equilibrium. Interestingly, magnonic spectral function can be substantially modified by acquiring additional peaks due to quasibound states of electrons and magnons once the interaction between these subsystems is turned on. The Hamiltonian of fermions interacting with HP bosons gives an incorrect ground state and electronic spectral function unless a large number of terms are retained in the truncated HP transformation. Furthermore, tracking the nonequilibrium dynamics of localized spins over longer time intervals requires a progressively larger number of terms in truncated HP transformation, even if a small magnon density is excited initially, but the required number of terms is reduced when interaction with conduction electrons is turned on. Finally, we show that recently proposed [M. Vogl *et al.*, Phys. Rev. Res. **2**, 043243 (2020); J. König *et al.*, SciPost Phys. **10**, 007 (2021)] resummed HP transformation, where spin operators are expressed as polynomials in bosonic operators, resolves the trouble with truncated HP transformation while allowing us to derive an exact quantum many-body (manifestly Hermitian) Hamiltonian consisting of a *finite and fixed* number of boson-boson and electron-boson interacting terms.

DOI: 10.1103/PhysRevB.104.184425

I. INTRODUCTION

The concept of spin waves was introduced by Bloch [1] as a disturbance in the local magnetic ordering of ferromagnetic materials. In the spin wave, the expectation value of localized spin operators precess around the easy axis with the phase of precession of adjacent expectation values varying harmonically in space over the wavelength λ. The quanta of energy of spin waves behave as quasiparticles termed magnons, each of which carries energy $\hbar\omega$ and spin $\hbar$.

With regard to terminology, we note that in spintronics and magnonics [2] literature it is common to use "spin wave" for excitations described by the classical Landau-Lifshitz-Gilbert (LLG) equation [3] within numerical micromagnetics [4] or atomistic spin dynamics [5], while "magnon" is used for quantized version of the same excitation. In other subfields of condensed matter physics, the terms spin waves and magnons are sometimes used to distinguish between long- and short-wavelength excitations, respectively, or both names are used interchangeably [6].

The second-quantization description of magnons was introduced by Holstein and Primakoff (HP) [7] by mapping the localized spin operator $\hat{\mathbf{S}}_i$ on site i of the lattice to bosonic operators

$$\hat{S}_i^+ = \hat{S}_i^x + i\hat{S}_i^y = \sqrt{2S}\left(1 - \frac{\hat{n}_i}{2S}\right)^{1/2} \hat{a}_i, \tag{1a}$$

$$\hat{S}_i^- = \hat{S}_i^x - i\hat{S}_i^y = \sqrt{2S}\hat{a}_i^\dagger\left(1 - \frac{\hat{n}_i}{2S}\right)^{1/2}, \tag{1b}$$

$$\hat{S}_i^z = S - \hat{n}_i. \tag{1c}$$

*bnikolic@udel.edu

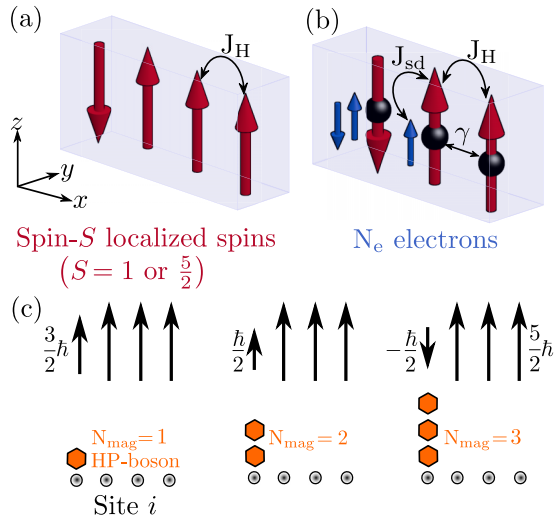

FIG. 1. (a) Schematic view of a finite-size 1D quantum many-body system comprised of a chain of $N = 4$ sites hosting spin-S localized spins ($S = 1$ or $S = \frac{5}{2}$ considered in this paper) which interact with each other via the nearest-neighbor Heisenberg exchange interaction of strength J_H. At $t = 0$, nonequilibrium dynamics can be initiated by flipping the localized spin on site $i = 1$. The 1D quantum many-body system in (b) is the same as (a) but with smaller number of $N = 3$ sites whose spin-S localized spins additionally interact with conduction electron spins (blue arrows) via the *sd* exchange interaction of strength J_{sd}. The conduction electrons hop between the sites with the hopping parameter γ where half-filled (i.e., $N_e = 3$) tight-binding chain is used. (c) illustrates the reduction of eigenvalues S_i^z of the z-component $\hat{S}_i^z$ of localized spin-$\frac{5}{2}$ operator on site $i = 1$ by N_{mag} units, which is *equivalent* to creating N_{mag} Holstein-Primakoff bosons on site $i = 1$ once the localized spins are mapped [7] to bosonic operators.

Here $\hat{a}_i^\dagger$ ($\hat{a}_i$) creates (annihilates) HP boson on site i and satisfies the bosonic commutation relations

$$[\hat{a}_i, \hat{a}_j^\dagger] = \mathbb{1}\delta_{ij}, \tag{2}$$

where $\mathbb{1}$ is the unit operator in the infinite dimensional Hilbert space of bosons. The HP boson number operator, $\hat{n}_i = \hat{a}_i^\dagger \hat{a}_i$, whose eigenvalues and eigenstates are defined by $\hat{n}_i|n\rangle = n|n\rangle$, measures how much the localized spin deviates away from the ground state (GS) [where the ferromagnetic GS with the z axis as the easy axis is assumed in Eqs. (1)]. Thus, the creation of one HP boson is equivalent to *removing one unit* of spin angular momentum from the GS [see Fig. 1(c) for illustration and Sec. II I for technical details].

Textbook literature [8,9] is typically focused on band structures of noninteracting magnons (which can also be topologically nontrivial [10,11]), so it discusses only the lowest-order truncation,

$$\hat{S}_i^+ \approx \sqrt{2S}\hat{a}_i, \tag{3a}$$

$$\hat{S}_i^- \approx \sqrt{2S}\hat{a}_i^\dagger, \tag{3b}$$

of the original HP transformation in Eqs. (1) while retaining the terms in the Hamiltonian that are up to the quadratic order in the bosonic operators. This effectively assumes low-density limit $\langle \hat{n}_i \rangle / 2S \ll 1$ achieved at, e.g., sufficiently low temperatures [12] and/or large $S \gg 1$ in which HP bosons can be treated as noninteracting. Taking into account higher order terms in the Hamiltonian generated by Eqs. (3), as well as in the Taylor expansion of the square root in Eqs. (1), produces higher-than-quadratic terms in the bosonic operators which describe *boson-boson interactions* [6,9,11–15], leading to renormalization of magnon energy, magnon decay (one magnon decays into two) [6], coalescence (two magnons coalesce into one), four-magnon interactions, decays into four magnons, and other higher order processes [16].

Since bosonic operators $\hat{a}_i^\dagger$, $\hat{a}_i$ act on an *infinite*-dimensional Hilbert space, and the physical Hilbert space corresponding to a single localized spin on site i is spanned by only $2S + 1$ states, the extra unphysical states are decoupled from the physical ones by the square root in Eqs. (1). Such exact HP transformation in Eqs. (1) splits the infinite dimensional Hilbert space spanned by boson number states $\{|n\rangle\}_{n\in\mathbb{N}}$ into two sectors—physical states $\{|n\rangle\}_{n=0,\ldots,2S}$; and all the unphysical ones $\{|n\rangle\}_{n>2S}$ [see also Eq. (36)]. Those sectors *cannot* be connected by $\hat{S}_i^+$ and $\hat{S}_i^-$ operators. However, when the square root in Eqs. (1) is expanded in a power series and then truncated (see Secs. II E and II F) to any *finite* order N_T, the physical and unphysical subspaces become coupled. In addition, canonical commutation relations for the spin operators are then satisfied only approximately, resulting in artificial breaking of rotational symmetries that may be present in the original Hamiltonian [17,18].

Retaining higher order terms in the Taylor series expansion of Eqs. (1) is necessary to study, e.g., equilibrium properties at increasing temperature [16,19,20] or nonequilibrium dynamics [13–15,21]. For example, Dyson [19] calculated how magnetization of the Heisenberg model of a three-dimensional ferromagnet decays with temperature, $M(T)/M(0) = 1 - c_0 T^{3/2} - c_1 T^{5/2} - c_2 T^{7/2} - c_3 T^4 + O(T^{9/2})$, where $T^{3/2}$ is the so-called Bloch law for noninteracting magnons with parabolic energy-momentum dispersion; second and third terms also stem from noninteracting magnons but with nonparabolic dispersion on a discrete lattice; and magnon-magnon interactions start manifesting at order T^4. In addition, exotic quantum matter like quantum spin liquids [22,23] *cannot* be studied by any order of Taylor series expansion of Eqs. (1) due to their highly entangled GS and absence of long-range order. Calculations of this type [19,23] require many-body perturbation theory (MBPT) [23–25], which is most easily formulated in terms of bosonic or fermionic operators. For such operators, the Wick theorem [26] for their averages over the noninteracting system makes it possible to expand properties of the interacting system into the Feynman diagrammatic series of perturbation order $O(g^n)$, where g is the strength of fermion-boson interaction.

The necessity for mapping spin operators to bosonic or fermionic ones stems from the fact that spin operators satisfy neither fermionic nor bosonic commutation relations. For example, the Pauli matrices for $S = 1/2$ commute on different sites and anticommute on the same site. The commutation relations for spins are determined by SU(2) algebra, leading to the absence of a Wick theorem for the generators. To avoid this difficulty and construct a diagrammatic MBPT or path integrals [21] for quantum spin systems, a variety of approaches have been developed. Since higher order terms in

the power-series expansion of the square root in the HP transformation in Eqs. (1), conjectured by Kubo [27] to be only an asymptotic series, lead to cumbersome MBPT [28,29], a plethora of other mappings of original localized spin operators to bosonic or fermionic operators has been proposed, such as mappings to Dyson-Maleev bosons [19,30], Schwinger bosons [21], fermions [31,32], Majorana fermions [33], supersymmetric operators [34], and exotic particles called semions [35].

However, all of them possess some drawbacks. While the Dyson-Maleev transformation evades usage of the square root of operators in Eqs. (1), it generates a Hamiltonian that is *not manifestly Hermitian*. The Schwinger transformation requires the introduction of auxiliary fields. The Jordan-Wigner transformation [31] or mapping to Majorana fermions [33] are exact, but they work only for $S = 1/2$ operators. Although the mapping of localized spin operators to bosonic or fermionic operators can be evaded altogether in the path integral formulation by using spin coherent states, this approach leads to topological terms associated with the Berry phase, so even in path integral formalism mapping to bosonic operators is preferred [21].

These drawbacks have prompted very recent reexaminations [17,18] of HP transformation to find possible nonperturbative replacements of the Taylor series of the square root in Eqs. (1) which can be written as a polynomial in bosonic operators, while ensuring no coupling between physical and unphysical subspaces as well as *manifestly Hermitian* bosonic Hamiltonian. Although such polynomial expressions do not exactly reproduce the canonical commutation relations for the spin operators, the extra terms generated turn out to be unimportant because they do not couple physical and unphysical subspaces of the bosonic Hilbert space, i.e., they act solely on the unphysical subspace [17,18].

The MBPT calculations of equilibrium magnon properties based on Dyson-Maleev versus truncated HP transformation have been carefully compared in the literature over many decades [28,29]. On the other hand, much less is known about the range of validity [36,37] of truncated HP transformation when describing nonequilibrium dynamics of localized spins, including situations where *additional interactions with conduction electrons* are present. The electron–localized-spin interactions are frequently encountered in quantum transport phenomena in spintronics. The nonequilibrium MBPT [24,25] for such problems is virtually always conducted using truncated HP transformation, as exemplified by theoretical and computational modeling of inelastic electron tunneling spectroscopy in magnetic tunnel junctions [38]; spin-transfer [39–42] and spin-orbit torques [43]; ultrafast demagnetization [44]; and conversion of magnonic spin currents into electronic spin current (or vice versa) at magnetic-insulator/normal-metal interfaces [45–47]. Similarly, truncated HP transformation is typically chosen for problems in quantum magnonics, such as for nonequilibrium dynamics of localized spins within magnetic insulators [13–15,48]; their interaction with electromagnetic fields [12,49]; and analysis of coherence of magnon quantum states [14,50]. With certainty, one can expect that truncated HP transformation will break down at sufficiently long times (as confirmed in Figs. 4–6 and 11) when higher-order terms in the expansion of the square root in HP transformation become important, but details of such breakdown—i.e., *how many terms are needed to ensure exact time evolution over experimentally relevant time interval* [see Fig. 5]—remain unexplored. Such breakdown precludes [39,42] accurate tracking of nonequilibrium dynamics of localized spins, which can be driven far from their initial direction (along the easy axis) and eventually reversed by, e.g., spin-transfer torque [51,52].

Instead, current-driven magnetization reversal via spin-transfer torque [51] is standardly modeled by the LLG equation [53], which is combined in a multiscale fashion with some type of steady-state [54] or time-dependent quantum transport calculations [55–61] considering single-particle quantum Hamiltonians for electrons. Thus, such hybrid quantum-classical theories are justified only in the classical limit $\hbar \to 0$ and for large localized spins $S \to \infty$ (while $\hbar S \to 1$) [3,60,62,63], as well as in the absence of entanglement [3,52,63,64] between quantum states of localized spins. For example, in the emerging concept of quantum spin torque [52,64–67], describing transfer of angular momentum between spins of flowing electrons and localized spins in situations [68] where the latter *must* be described by quantum-mechanical operators, the whole system of electrons and localized spins can only be modeled by a quantum many-body Hamiltonian [as exemplified by Eqs. (4) and (72)].

In this paper, we apply exact diagonalization techniques [69] to the quantum many-body Hamiltonians defined on a one-dimensional (1D) chain of N sites hosting fermionic (for electrons) and localized spin operators or fermionic and bosonic (obtained by mapping the original localized spin operators) operators. By comparing their many-body quantum states and Green's functions (GFs), both in *equilibrium* and in *nonequilibrium*, makes it possible to precisely delineate *the range of validity of truncated HP transformation*. We consider a 1D quantum Heisenberg ferromagnetic spin-S XXX chain hosting localized spins which interact via the nearest-neighbor (NN) exchange interaction of strength J_H, as illustrated in Fig. 1(a), where both spin $S = 1$ (as the ultraquantum limit) and $S = 5/2$ (as in, e.g., Fe^{3+} valence state with five $3d$ electrons coupled by Hund's rule into the high spin state forming a localized $S = 5/2$ moment) are employed. Naively, the eigenvalue of $\hat{\mathbf{S}}_i^2$ being $S^2(1 + 1/S)$ suggests that quantum effects become progressively less important for $S > 1$, but they exist for all $S < \infty$ vanishing as $1/2S$ in the classical limit [70]. The nonzero electron hopping γ between the sites, where $N = 3$ sites are chosen when electrons are present as illustrated in Fig. 1(b), means that such 1D chain models a ferromagnetic metal. Its N_e conduction electrons [we consider a half-filled lattice, so $N_e = 3$ for systems in Fig. 1(b)] interact with localized spins via *sd* exchange interaction [71] usually considered in spintronics. From the viewpoint of the physics of strongly correlated electrons, the model illustrated in Fig. 1(b) can also be interpreted as the Kondo-Heisenberg chain [72].

For technical reasons (i.e., exponential increase of the size of matrix representation of Hamiltonian), we consider 1D chains of $N \leqslant 7$ sites while concentrating on *generic features* which are not bound to one dimension or a small number of electrons and localized spins considered. In fact, artificial atomic chains that realize our model have been fab-

ricated in experiments by using ferromagnetically [73] or antiferromagnetically [74] coupled Fe atoms on a substrate, where magnons along the chain are excited and detected via atom-resolved inelastic tunneling spectroscopy in a scanning tunneling microscope [73].

It is also worth recalling that small clusters (composed of, e.g., two to eight lattice sites) in one, two, and three spatial dimensions—hosting electrons interacting with each other via the on-site or NN Coulomb interaction [75–78] (as described by pure and extended Hubbard models [75], respectively) or electrons interacting with bosons [79–81]—play an important role in testing approximation schemes for quantum many-body problems against numerically exact benchmarks in different subfields of condensed matter and atomic-molecular-optical physics. Furthermore, the advent of numerically exact algorithms and supercomputers has led to recent re-examination of many physically motivated simplifications and approximations developed earlier in quantum many-body theory for condensed matter systems (such as Migdal-Eliashberg theory for electron-phonon systems [82], partial summation of classes in Feynman diagrams in MBPT [83], and existence of Luttinger-Ward functional of dressed one-particle GF [84]) to draw boundaries of parameters for which their complete breakdown ensues.

Our study proceeds in the same spirit, where we *explicitly delineate breakdown times*—in Figs. 4 and 5 for localized spins alone and in Figs. 6 and 11 for localized spins interacting with conduction electrons—at which widely used in spintronics and magnonics truncated versions of the HP transformation in Eqs. (1) inevitably break down by generating quantum time evolution which starts to substantially deviate from the exact one obtained by using the original localized spin operators.

The paper is organized as follows. In Sec. II, we introduce different versions of quantum many-body Hamiltonians describing systems in Fig. 1 and their matrix representations as well as a procedure to obtain the exact one-particle double-time-dependent retarded and lesser GFs. In particular, Sec. II E introduces an infinite power series expansion of the HP transformation from Eqs. (1) and its truncation, while Sec. II F provides a brief summary of recently proposed [17,18] resummation of truncated HP transformation. The time evolution of quantum many-body states of a spin chain with no electrons ($N_e = 0$) is employed in Sec. III A to examine the range of validity of truncated HP transformation when tracking time evolution of localized spins in the presence of *magnon-magnon* interaction and different numbers of initially excited magnons $N_{\rm mag}$. Then, in Sec. III B we introduce electrons into a 1D chain to examine the range of validity of truncated HP transformation when tracking time evolution of localized spins in the presence of *both* magnon-magnon and electron-magnon interactions. In the same Sec. III B, we additionally employ resummation [17,18] of truncated HP transformation to derive quantum many-body Hamiltonian [Eq. (72)] for electron-magnon systems in terms of fermionic and bosonic operators whose usage reproduces a numerically exact result from calculations based on the original localized spin operators. In Secs. III C and III D, we compare GS and electronic spectral function (or interacting density of states [85,86]) of a quantum many-body Hamiltonian in terms of the original localized spin operators versus a Hamiltonian using bosonic operators generated by truncated HP transformation. The magnonic spectral function and related excited eigenstates are studied in Sec. III E. Since both ground and excited states of electron-magnon interacting systems are many-body entangled [87], we compute their entanglement entropy in Sec. III F which makes it possible to quantify how far they are from the eigenstates of a system where the interaction between electrons and localized spins is turned off. Finally, Sec. III G studies the time evolution of diagonal and off-diagonal elements of time-dependent lesser electronic and magnonic GFs while using both exact, truncated, and resummed HP transformation to clarify that, computationally, the often-employed local self-energy approximation [88–91] (i.e., neglecting the off-diagonal elements) for electron-boson interacting systems is generally not justified. We conclude in Sec. IV.

II. MODELS AND METHODS

A. Quantum many-body Hamiltonian of electrons interacting with localized spins

The quantum many-body Hamiltonian of a 1D chain composed of N sites (with open boundary conditions assumed), each of which hosts spin-S localized spins interacting with spins of conduction electrons [as illustrated in Fig. 1(b)] is given by [38,92]

$$\hat{H} = \hat{H}_e + \hat{H}_{\rm lspins} + \hat{H}_{e-{\rm lspins}}. \tag{4}$$

It acts in the total space $\mathcal{F}_e \otimes \mathcal{H}_{\rm lspins}$, which is a tensor product of the Fock space of electrons, $\mathcal{F}_e$, and the Hilbert space of all localized spins:

$$\mathcal{H}_{\rm lspins} = \mathcal{H}_1 \otimes \cdots \otimes \mathcal{H}_N. \tag{5}$$

The Fock space of electrons [25],

$$\mathcal{F}_e = \overline{\mathbb{C} \oplus \mathcal{H}_e \oplus \hat{\mathcal{A}}(\mathcal{H}_e \otimes \mathcal{H}_e) \oplus \hat{\mathcal{A}}(\mathcal{H}_e \otimes \mathcal{H}_e \otimes \mathcal{H}_e) \oplus \cdots}, \tag{6}$$

is induced by the one-electron Hilbert space $\mathcal{H}_e$ as the completion (indicated by overline) of the direct sum of antisymmetrized n-fold tensor products of $\mathcal{H}_e$. The operator $\hat{\mathcal{A}}$ antisymmetrizes tensors for fermionic particles. In the sector of $\mathcal{F}_e \otimes \mathcal{H}_{\rm lspins}$ with $N_e = 0$ electrons, we have a 1D chain hosting only spin-S localized spins [as illustrated in Fig. 1(a)], which is described solely by

$$\hat{H}_{\rm lspins} = -J_H \sum_{\langle ij \rangle} \hat{\mathbf{S}}_i \cdot \hat{\mathbf{S}}_j, \tag{7}$$

chosen as the quantum Heisenberg Hamiltonian with the NN exchange interaction (as signified by $\langle ij \rangle$ notation) of strength $J_H = 1$ eV. When electrons are present, they are described by

$$\hat{H}_e = -\gamma \sum_{\langle ij \rangle} \hat{\psi}_i^\dagger \hat{\psi}_j, \tag{8}$$

chosen as the tight-binding Hamiltonian with the NN hopping $\gamma = 1$ eV between orbitals centered on each site i that are orthogonal to each other. The Hamiltonian describing *sd* exchange interaction of strength $J_{\rm sd}$ [71] between conduction

electron spin and localized spins is given by

$$\hat{H}_{e-\text{lspins}} = -J_{\text{sd}} \sum_{i=1}^{N} \hat{\psi}_i^\dagger \hat{\boldsymbol{\sigma}} \hat{\psi}_i \cdot \hat{\mathbf{S}}_i. \tag{9}$$

The row vector operator $\hat{\psi}_i^\dagger = (\hat{\psi}_{i\uparrow}^\dagger, \hat{\psi}_{i\downarrow}^\dagger)$ consists of operators $\hat{\psi}_{i\sigma}^\dagger$ which create an electron with spin $\sigma = \uparrow, \downarrow$ on site i; $\hat{\psi}_i$ is a column vector operator that contains the corresponding annihilation operators and $\hat{\boldsymbol{\sigma}} = (\hat{\sigma}^x, \hat{\sigma}^y, \hat{\sigma}^z)$ is the vector of the 2×2 Pauli spin matrices as matrix representation of spin-$\frac{1}{2}$ operator of electronic spin.

Using notation $\{\hat{O}_1, \hat{O}_2\}$ for the anticommutator and $[\hat{O}_1, \hat{O}_2]$ for the commutator of two operators $\hat{O}_1$ and $\hat{O}_2$, fermionic operators of electrons satisfy

$$\{\hat{\psi}_{i\sigma}, \hat{\psi}_{j\sigma'}^\dagger\} = \mathbb{1}\delta_{ij}\delta_{\sigma\sigma'}, \tag{10}$$

where $\mathbb{1}$ is the unit operator in the Fock space $\mathcal{F}_e$. The localized spin operators $\hat{S}_i^\alpha$ ($\alpha = x, y, z$) on site i satisfy the angular momentum algebra:

$$\left[\hat{S}_i^x, \hat{S}_j^y\right] = \mathrm{i}\hat{S}_i^z\delta_{ij}, \tag{11a}$$

$$\left[\hat{S}_i^y, \hat{S}_j^z\right] = \mathrm{i}\hat{S}_i^x\delta_{ij}, \tag{11b}$$

$$\left[\hat{S}_i^z, \hat{S}_j^x\right] = \mathrm{i}\hat{S}_i^y\delta_{ij}. \tag{11c}$$

The square of the localized spin operator, $\hat{S}_i^2 = (\hat{S}_i^x)^2 + (\hat{S}_i^y)^2 + (\hat{S}_i^z)^2$, commutes with each component:

$$\left[\hat{S}_i^2, \hat{S}_j^\alpha\right] = 0. \tag{12}$$

For computational convenience in calculations of electronic GFs, we change [93] the basis of one-particle electronic states from site basis to eigenenergy basis to obtain

$$\hat{H}_e = \sum_{i=1}^{N} \epsilon_i \hat{c}_i^\dagger \hat{c}_i, \tag{13}$$

where $\hat{c}_i^\dagger = (\hat{c}_{i\uparrow}^\dagger, \hat{c}_{i\downarrow}^\dagger)$ is a row vector consisting of $\hat{c}_{i\sigma}^\dagger$ operators which create an electron with spin $\sigma = \uparrow, \downarrow$ in one-particle electronic eigenstate $|\epsilon_i\rangle$ with the discrete eigenenergy ϵ_i, so $\hat{H}_e |\epsilon_i\rangle = \epsilon_i |\epsilon_i\rangle$. These eigenenergies and eigenstates are evaluated by diagonalizing the one-particle tight-binding Hamiltonian

$$\hat{H}_e = \sum_{\langle ij \rangle} -\gamma \, |i\rangle \langle j| \,, \tag{14}$$

where $|i\rangle$ denotes an orbital [whose coordinate representation is $\langle \mathbf{r}|i\rangle = \phi(\mathbf{r} - \mathbf{R}_i)$] of an electron centered on site i such that $\langle i|j\rangle = \delta_{ij}$. Using change of basis transformation rules for operators in second-quantization formalism,

$$\hat{\psi}_{i\sigma} = \sum_{j=1}^{N} \langle i|\epsilon_j\rangle \, \hat{c}_{j\sigma} \,, \tag{15}$$

and substituting this into Eq. (9), we get

$$\hat{H}_{e-\text{lspins}} = -J_{\text{sd}} \sum_{i=1}^{N} \sum_{j=1}^{N} \sum_{j'=1}^{N} \langle \epsilon_{j'}|i\rangle \, \langle i|\epsilon_j\rangle \, \hat{c}_{j'}^\dagger \hat{\boldsymbol{\sigma}} \hat{c}_j \cdot \hat{\mathbf{S}}_i. \tag{16}$$

Since each $\hat{c}_{i\sigma}^\dagger$ or $\hat{c}_{i\sigma}$ operator is represented by 4×4 matrix (see Sec. II C), and each $\hat{\mathbf{S}}_i$ operator is represented by a $(2S+1) \times (2S+1)$ matrix, the quantum many-body Hamiltonian in Eq. (4) for the chain of N sites in Fig. 1(b) is represented by a matrix of size $[4^N \times (2S+1)^N] \times [4^N \times (2S+1)^N]$. Although systems containing larger than our choice $N = 3$ (when electrons are present) or $N \leqslant 7$ (when electrons are absent) sites could be diagonalized with state-of-the-art numerical algorithms [69], we restrict our analysis to such smaller number of sites to make the analysis transparent and pedagogical—for example, Figs. 7 and 9 provide easy-to-follow visualization of ground and excited quantum many-body states depicting population of a small number of energy levels ϵ_i, respectively.

B. Symmetries of quantum many-body Hamiltonian

The exact diagonalization of the quantum many-body Hamiltonian in Eq. (4),

$$\hat{H} \, |\Psi_k\rangle = E_k \, |\Psi_k\rangle \,, \tag{17}$$

yields its many-body eigenenergies E_k and many-body eigenstates $|\Psi_k\rangle$. The total electron number operator is given by

$$\hat{N}_e = \sum_{i=1}^{N} (\hat{c}_{i\uparrow}^\dagger \hat{c}_{i\uparrow} + \hat{c}_{i\downarrow}^\dagger \hat{c}_{i\downarrow}). \tag{18}$$

The operator of total spin in the z direction,

$$\hat{S}_{\text{tot}}^z = \frac{1}{2} \sum_{i=1}^{N} (\hat{c}_{i\uparrow}^\dagger \hat{c}_{i\uparrow} - \hat{c}_{i\downarrow}^\dagger \hat{c}_{i\downarrow}) + \sum_{i=1}^{N} \hat{S}_i^z, \tag{19}$$

is the sum of electronic spin operators (first term) and localized spin operators (second term) along the z axis at each site i. The many-body Hamiltonian in Eq. (4) has two symmetries encoded by the commutation relations

$$[\hat{H}, \hat{N}_e] = 0, \tag{20}$$

which is due to conservation of the number of electrons N_e, and

$$\left[\hat{H}, \hat{S}_{\text{tot}}^z\right] = 0, \tag{21}$$

which is due to conservation of total z spin (electronic + localized spin) S_{tot}^z. Therefore, N_e and S_{tot}^z, as eigenvalues of $\hat{N}_e$ and $\hat{S}_{\text{tot}}^z$, respectively, serve as good quantum numbers for labeling quantum many-body eigenstates,

$$|\Psi_k\rangle = \left|E_k, N_e, S_{\text{tot}}^z\right\rangle, \tag{22}$$

together with many-body eigenenergy E_k.

The effect of two symmetries in Eqs. (20) and (21) can also be visualized in the matrix representation (see Secs. II C and II D) of quantum many-body Hamiltonian $\hat{H}$ [Eq. (4)]. For example, in Fig. 2(a) the matrix elements of $\hat{H}$ in the original site basis are visually scattered throughout the whole matrix. However, when $\hat{H}$ is represented in the basis of eigenstates of $\hat{N}_e$, Fig. 2(b) shows that its matrix becomes block diagonal where each block contains the nonzero matrix elements associated with states with fixed number of electrons N_e. Finally, in Fig. 2(c), $\hat{H}$ is represented in the basis composed of eigenstates of $\hat{N}_e$ and $\hat{S}_{\text{tot}}^z$ simultaneously, which isolates additional submatrices with fixed S_{tot}^z within blocks associated to fixed N_e.

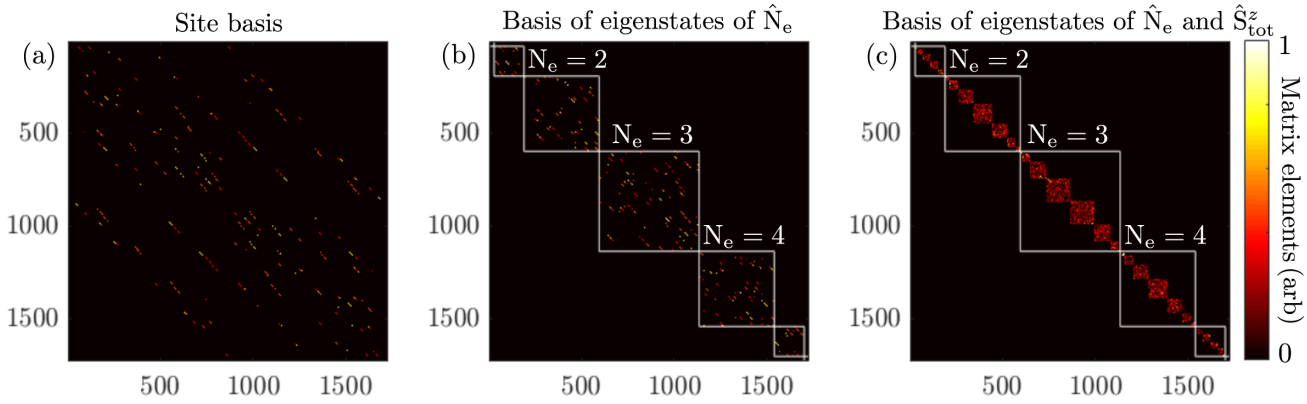

FIG. 2. Visualization of the absolute value of matrix elements of Hamiltonian $\hat{H}$ [Eq. (4)] for 1D quantum many-body system of N_e conduction electrons interacting with localized spins $S = 1$ illustrated in Fig. 1(b). The matrix representation of $\hat{H}$ is given: (a) in site basis; (b) in basis composed of eigenstates of electron number operator $\hat{N}_e$ [Eq. (18)], so each block consists of states with fixed number of electrons N_e ($N_e = 2, 3, 4$ is marked explicitly); and (c) in basis composed of eigenstates of *both* $\hat{N}_e$ [Eq. (18)] and total z-spin operator $\hat{S}^z_{\text{tot}}$ [Eq. (19)].

C. Matrix representation of electronic creation and annihilation operators

A fermionic operator creating or annihilating electrons on a single site operate within the natural basis of kets $|0\rangle$, $|\uparrow\rangle$, $|\downarrow\rangle$, and $|\uparrow\downarrow\rangle$, which denote the empty state, state with one spin-$\uparrow$ electron, state with one spin-$\downarrow$ electron, and the state with one spin-$\uparrow$ and one spin-$\downarrow$ electron. Thus, these basis states are represented by column vectors

$$|0\rangle = \begin{pmatrix}1\\0\\0\\0\end{pmatrix}, \ |\uparrow\rangle = \begin{pmatrix}0\\1\\0\\0\end{pmatrix}, \ |\downarrow\rangle = \begin{pmatrix}0\\0\\1\\0\end{pmatrix}, \ |\uparrow\downarrow\rangle = \begin{pmatrix}0\\0\\0\\1\end{pmatrix}. \tag{23}$$

In the same basis, creation and annihilation operators that act in the one-site or two-particle subspace $\mathscr{H}_{N=1} = \hat{\mathcal{A}}(\mathcal{H}_e \otimes \mathcal{H}_e)$ of the Fock space $\mathcal{F}_e$ are represented by 4×4 matrices

$$\hat{\psi}^\dagger_\uparrow = \begin{pmatrix}0&0&0&0\\1&0&0&0\\0&0&0&0\\0&0&1&0\end{pmatrix}, \hat{\psi}^\dagger_\downarrow = \begin{pmatrix}0&0&0&0\\0&0&0&0\\1&0&0&0\\0&-1&0&0\end{pmatrix},$$

$$\hat{\psi}_\sigma = [\hat{\psi}^\dagger_{1\sigma}]^T, \tag{24}$$

which satisfy the fermionic commutation relations in Eq. (10). If we consider two sites, then electronic creation (annihilation) operators, $\hat{\psi}^\dagger_1$ ($\hat{\psi}_1$) and $\hat{\psi}^\dagger_2$ ($\hat{\psi}_2$), act in the two-site or four-particle subspace $\mathscr{H}_{N=2} = \hat{\mathcal{A}}(\mathcal{H}_e \otimes \mathcal{H}_e \otimes \mathcal{H}_e \otimes \mathcal{H}_e)$ of the Fock space $\mathcal{F}_e$ and are represented by matrices of size $4^2 \times 4^2$. For example, the action of $\hat{\psi}^\dagger_{1\sigma}$ in $\mathscr{H}_{N=2}$ is given by

$$(\hat{\psi}^\dagger_{1\sigma})_{\mathscr{H}_{N=2}} = \hat{\psi}^\dagger_\sigma \otimes \mathbb{1}, \tag{25}$$

where $\mathbb{1}$ is a 4×4 unit matrix. However, the action of $(\hat{\psi}^\dagger_{2\sigma})_{\mathscr{H}_{N=2}}$

$$(\psi^\dagger_{2\sigma})_{\mathscr{H}_{N=2}} = \hat{P} \otimes \hat{\psi}^\dagger_\sigma. \tag{26}$$

requires [93] the permutation matrix $\hat{P} = \text{diag}(1, -1, -1, 1)$, instead of naïvely using only the unit matrix $\mathbb{1}$ to preserve the correct anticommutation relations of fermionic operators at different sites in Eq. (10). The next step is to construct the matrix representation of electronic creation and annihilation operators for three sites, which is done in a similar fashion [93] to furnish

$$(\hat{\psi}^\dagger_{1\sigma})_{\mathscr{H}_{N=3}} = \hat{\psi}^\dagger_\sigma \otimes \mathbb{1} \otimes \mathbb{1}, \tag{27a}$$

$$(\hat{\psi}^\dagger_{2\sigma})_{\mathscr{H}_{N=3}} = \hat{P} \otimes \hat{\psi}^\dagger_\sigma \otimes \mathbb{1}, \tag{27b}$$

$$(\hat{\psi}^\dagger_{3\sigma})_{\mathscr{H}_{N=3}} = \hat{P} \otimes \hat{P} \otimes \hat{\psi}^\dagger_\sigma, \tag{27c}$$

where each operator on the left-hand side (LHS) is a $4^3 \times 4^3$ matrix. Equations (27) also make it clear how to inductively construct the matrix representations of electronic creation and annihilation operators for arbitrary number of sites N, where these operators act in $\mathscr{H}_N = \hat{\mathcal{A}}(\underbrace{\mathcal{H}_e \otimes \mathcal{H}_e \cdots \mathcal{H}_e \otimes \mathcal{H}_e}_{2N \text{ times}})$ subspace of the Fock space $\mathcal{F}_e$. Note that the matrix representation in Eq. (27) can be directly linked to the states of $2N$ qubits by the Jordan-Wigner transformation [94] which is prevalent in simulating the Fermi-Hubbard models on quantum computers [95].

D. Localized spin operators

The matrix representation of localized spin operator $\hat{\mathbf{S}} = (\hat{S}^x, \hat{S}^y, \hat{S}^z)$ is given by

$$\langle m \pm 1| \hat{S}^x |m\rangle = \frac{1}{2}\sqrt{S(S+1) - m(m \pm 1)}, \tag{28a}$$

$$\langle m \pm 1| \hat{S}^y |m\rangle = \frac{1}{2i}\sqrt{S(S+1) - m(m \pm 1)}, \tag{28b}$$

$$\langle m| \hat{S}^z |m\rangle = m, \tag{28c}$$

where $|m\rangle$ is an eigenstate of $\hat{S}^z$; $m \in \{-S, -S+1, \cdots, S-1, S\}$; and $\hat{S}^\alpha$ is a $(2S+1) \times (2S+1)$ matrix acting in the single-site subspace $\mathcal{H}_i$ of $\mathcal{H}_{\text{lspins}}$. For the chain in Fig. 1(a) composed of N sites hosting spin-S localized spins, their operators act in the total space of all localized spins $\mathcal{H}_{\text{lspins}}$ [Eq. (5)] as

$$\hat{S}^\alpha_i = \underbrace{\mathbb{1} \otimes \mathbb{1} \cdots \mathbb{1} \otimes \mathbb{1}}_{i-1 \text{ times}} \otimes \hat{S}^\alpha \otimes \underbrace{\mathbb{1} \otimes \mathbb{1} \cdots \mathbb{1} \otimes \mathbb{1}}_{N-i \text{ times}}, \tag{29}$$

where $\mathbb{1}$ is now used to denote the $(2S+1)\times(2S+1)$ unit matrix.

E. Truncated Holstein-Primakoff transformation

The HP transformation shown in Eqs. (1) expresses localized spin operators in terms of bosonic operators. However, to make MBPT for such bosonic operators tractable [28,29], one typically expands the square root of Eqs. (1) in a power series in $x=\hat{n}_i/2S$,

$$(1-x)^{1/2}=\sum_{n=0}^{\infty}\frac{2n!}{4^n(1-2n)n!^2}x^n\approx\sum_{n=0}^{N_T}\frac{2n!}{4^n(1-2n)n!^2}x^n, \tag{30}$$

which is further truncated [9,11–15] to a finite number of terms N_T. Inserting this result in Eqs. (1), and using thus obtained $\hat{S}_i^{\alpha}$ in Eq. (7), we can rewrite

$$\hat{H}_{\text{lspins}}=\hat{H}_0+\hat{H}_{\text{int}}, \tag{31}$$

as the sum of two terms. Here

$$\hat{H}_0=-J_H(N-1)S^2+2J_HS\sum_{i=1}^{N}\hat{n}_i-J_HS\sum_{\langle ij\rangle}(\hat{a}_i^{\dagger}\hat{a}_j+\hat{a}_i\hat{a}_j^{\dagger}), \tag{32}$$

is the one-particle Hamiltonian of noninteracting HP bosons covered in textbook literature [8,9], whereas

$$\hat{H}_{\text{int}}=-J_H\sum_{\langle ij\rangle}\left[\hat{n}_i\hat{n}_j-\frac{\hat{a}_i\hat{a}_j^{\dagger}\hat{n}_j}{4S}-\frac{\hat{a}_i^{\dagger}\hat{n}_j\hat{a}_j}{4S}-\frac{\hat{n}_i\hat{a}_i\hat{a}_j^{\dagger}}{4S}-\frac{\hat{a}_i^{\dagger}\hat{n}_i\hat{a}_j}{4S}+\frac{\hat{n}_i\hat{a}_i\hat{a}_j^{\dagger}\hat{n}_j}{16S^2}+\frac{\hat{a}_i^{\dagger}\hat{n}_i\hat{n}_j\hat{a}_j}{16S^2}\right]+\cdots, \tag{33}$$

is composed of many-particle interacting terms that we write explicitly for truncation number $N_T=1$ to emphasize how nontrivial multiboson interactions arise even in this lowest order truncated HP transformation.

The bosonic operator $\hat{a}^{\dagger}$ is represented by an infinite dimensional matrix

$$\hat{a}^{\dagger}=\begin{pmatrix}0&0&0&\cdots&0&\cdots\\ \sqrt{1}&0&0&\cdots&0&\cdots\\ 0&\sqrt{2}&0&\cdots&0&\cdots\\ 0&0&\sqrt{3}&\ddots&\vdots&\cdots\\ 0&0&0&\sqrt{n}&0&\cdots\\ \vdots&\vdots&\vdots&\vdots&\vdots&\ddots\end{pmatrix}, \tag{34}$$

for a single site, so matrix representation of $\hat{a}_i^{\dagger}$ in the case of N sites is given by

$$\hat{a}_i^{\dagger}=\underbrace{\mathbb{1}\otimes\mathbb{1}\cdots\mathbb{1}\otimes\mathbb{1}}_{i-1\text{ times}}\otimes\hat{a}^{\dagger}\otimes\underbrace{\mathbb{1}\otimes\mathbb{1}\cdots\mathbb{1}\otimes\mathbb{1}}_{N-i\text{ times}}, \tag{35}$$

where $\mathbb{1}$ is the unit matrix of the same size as $\hat{a}^{\dagger}$. The matrix representation of operator $\hat{a}_i$ is the Hermitian conjugate of $\hat{a}_i^{\dagger}$.

F. Resummed Holstein-Primakoff transformation

In numerical calculations, $\hat{a}^{\dagger}$ or $\hat{a}$ are first truncated to finite $N_B\times N_B$ matrices, so the matrix representation of localized spin operators

$$\hat{S}^{\pm,z}=\begin{pmatrix}\hat{S}^{\pm,z}_{\text{phys}}&\Delta_{\text{c}}\\ \Delta_{\text{c}}^{\dagger}&\hat{S}^{\pm,z}_{\text{unphys}}\end{pmatrix}, \tag{36}$$

is then composed of matrix blocks associated with physical states $\{|n\rangle\}_{n=0,\cdots,2S}$ and unphysical states $\{|n\rangle\}_{n=2S+1,\cdots,N_B-1}$. Here Δ_{c} is the matrix block which couples physical and unphysical states. The numerically exact computation of the square root of an operator in Eqs. (1) ensures $\Delta_{\text{c}}=0$, but the Taylor series expansion of square root in Eq. (30) leads to $\Delta_{\text{c}}\neq 0$. This feature signals the trouble with the truncated HP transformation.

Alternatively, Refs. [17,18] have recently proposed a *resummed HP transformation* that furnishes a polynomial expansion for the square root in Eqs. (1)

$$\hat{S}_i^{+}\approx\sqrt{2S}\left[\sum_{n=0}^{N_{\max}}Q_n(\hat{a}_i^{\dagger})^n(\hat{a}_i)^n\right]\hat{a}_i, \tag{37}$$

where the iterative relation for coefficients Q_n,

$$Q_n=\frac{1}{n!}\left(1-\frac{n}{2S}\right)^{1/2}-\sum_{m=0}^{n-1}\frac{Q_m}{(n-m)!}, \tag{38}$$

was derived in Ref. [17] by using flow equations, whereas an equivalent closed-form expression

$$Q_n=\sum_{k=0}^{n}(-1)^{n-k}\frac{1}{k!\,(n-k)!}\left(1-\frac{k}{2S}\right)^{1/2} \tag{39}$$

was derived in Ref. [18] by using the Newton-series expansion. Equation (37) ensures that for $N_{\max}=2S$ the matrix-block $\hat{S}^{\pm,z}_{\text{phys}}$ associated with the physical states is *exact*, whereas coupling between the physical and unphysical states is $\Delta_{\text{c}}=0$, which makes nonzero submatrix $\hat{S}^{\pm,z}_{\text{unphys}}$ irrelevant for all practical purposes.

G. Relationship between localized spin operators and their mapping to Holstein-Primakoff bosons

For physically transparent understanding of the relationship between localized spin operators and their mapping to HP bosons, let us consider an example of a 1D chain of $N=5$ sites hosting spin-$\frac{5}{2}$ localized spins. We use arrows of different lengths

$$\left|\downarrow,\downarrow,\downarrow,\uparrow,\uparrow,\uparrow\right\rangle, \tag{40}$$

to denote eigenvalues S_i^z of localized spin operator $\hat{S}_i^z$ [Eq. (28c)] with $m=-5/2,\ -3/2,\ -1/2,\ 1/2,\ 3/2,\ 5/2$, respectively, as illustrated in Fig. 1(c). The ferromagnetic GS of this system,

$$\left|\uparrow\uparrow\uparrow\uparrow\uparrow\uparrow\right\rangle\equiv|0\rangle\,, \tag{41}$$

is identical to HP bosonic vacuum state $|0\rangle$ with zero HP bosons on each site $n_i=0$ and, therefore, total number of HP bosons

$$N_{\text{mag}}=\sum_i n_i, \tag{42}$$

also being zero, $N_{\rm mag} = 0$. Inside the ket vector on the LHS of Eq. (41), we indicate eigenstate with eigenvalue $m = 5/2$ of the localized spin operator $\hat{S}_i^z$ for all sites $i = 1$ to $i = 5$. Equation (41) is proved by noting that $|0\rangle$ on the right-hand side (RHS) of Eq. (41) and the ket on the LHS of Eq. (41) are both eigenstates of the same operator $\hat{S}_i^z$ with eigenvalue $m = 5/2$, i.e.,

$$\hat{S}_i^z \left|\uparrow\uparrow\uparrow\uparrow\uparrow\right\rangle = \frac{5}{2}\left|\uparrow\uparrow\uparrow\uparrow\uparrow\right\rangle, \tag{43a}$$

$$\hat{S}_i^z\,|0\rangle = (5/2 - \hat{n}_i)\,|0\rangle = 5/2\,|0\rangle\,, \tag{43b}$$

so they must be identical. Thus, creating $n_i = 1$ or $n_i = 2$ HP bosons on site $i = 1$, which we depict by

$$\hat{a}_1^\dagger\,|0\rangle = \left|\uparrow\uparrow\uparrow\uparrow\uparrow\right\rangle, \tag{44}$$

$$(\hat{a}_1^\dagger)^2\,|0\rangle = \left|\uparrow\ \uparrow\uparrow\uparrow\uparrow\right\rangle, \tag{45}$$

respectively, corresponds to reducing the size of localized spin on site $i = 1$ by one or two units of $\hbar$, i.e., $m = 5/2 \mapsto 3/2$ in Eq. (44) and $m = 5/2 \mapsto 1/2$ in Eq. (45). Similarly, the state with a total of $N_{\rm mag} = 2$ HP bosons created on different sites $i = 1$ and $i = 3$ is depicted by

$$\hat{a}_1^\dagger\hat{a}_3^\dagger\,|0\rangle = \left|\uparrow\uparrow\uparrow\uparrow\uparrow\right\rangle. \tag{46}$$

Thus, the creation of a total of $N_{\rm mag} \in 0, 1, 2, \ldots$ [Eq. (42)] HP bosons is interpreted physically as the reduction of the total localized z spin by $N_{\rm mag}$ units. Since in quantum state $(\hat{a}_i^\dagger)^n|0\rangle$ the expectation value of the z component of localized spin operator is $\langle\hat{S}_i^z\rangle = S - n$, the constraint $0 \leqslant n \leqslant 2S$ (i.e., at a given site i one *cannot* create more than $2S$ HP bosons) must be obeyed to remain in the subspace of physical states [Eq. (36)].

H. Numerically exact time evolution of quantum many-body states

The solution of the time-dependent Schrödinger equation for quantum many-body state $|\Psi(t)\rangle$,

$$i\hbar\frac{d\,|\Psi(t)\rangle}{dt} = \hat{H}(t)\,|\Psi(t)\rangle\,, \tag{47}$$

is formally given by

$$|\Psi(t+\delta t)\rangle = \mathcal{T}\exp\left(-\frac{i}{\hbar}\int_t^{t+\delta t} dt'\hat{H}(t')\right)|\Psi(t)\rangle\,, \tag{48}$$

where $\mathcal{T}$ is the time-ordering operator. While many numerical algorithms are available to propagate Eq. (48), including direct computation of matrix exponential when $\hat{H}$ is time independent, in general, by using sufficiently small δt and by considering $\hat{H}(t)$ to be constant over such δt, the Crank-Nicolson algorithm

$$\left(1 + \frac{i\delta t}{2\hbar}\hat{H}(t)\right)|\Psi(t+\delta t)\rangle = \left(1 - \frac{i\delta t}{2\hbar}\hat{H}(t)\right)|\Psi(t)\rangle\,, \tag{49}$$

we employ offers a propagation scheme that is unitary, accurate to second order in δt, and unconditionally stable [96]. In our simulations, $\delta t = 0.01$ fs has been used.

Using thus obtained $|\Psi(t)\rangle$, the time evolution of the expectation value of the α component of the localized spin operator on site i is given by

$$\langle\hat{S}_i^\alpha\rangle(t) = \langle\Psi(t)|\,\hat{S}_i^\alpha\,|\Psi(t)\rangle\,. \tag{50}$$

When localized spin operators are represented directly by finite size matrices in Eqs. (28) and (29), the corresponding expectation values $\langle\hat{S}_i^\alpha\rangle$ are *numerically exact* and, therefore, serve as a benchmark for alternative computation of the same expectation value when $\hat{S}_i^\alpha$ are represented by polynomial expressions in bosonic operators introduced in Secs. II E and II F.

I. From Holstein-Primakoff bosons to one- or two-magnon Fock states

In contrast to HP bosons created on a given site, $\hat{a}_i^\dagger|0\rangle$, which are not the eigenstates of $\hat{H}_0$ in Eq. (32), one-magnon states are linear combinations of $\hat{a}_i^\dagger|0\rangle$ which diagonalize Hamiltonian $\hat{H}_0$ (but with periodic boundary conditions included):

$$\hat{H}_0|q\rangle = [E_0 + \hbar\omega(q)]|q\rangle. \tag{51}$$

Thus, a magnon can be visualized as a bosonic quasiparticle that is completely "delocalized" over all sites while it carries momentum $\hbar q$ (assuming 1D chains we use in examples) and angular momentum $\hbar$. Here $E_0 = -2J_H S^2 N$ is the GS energy of a ferromagnetic spin chain.

To find explicit expression for excited eigenstate $|q\rangle$, we consider a 1D chain [Fig. 1(a)] composed of N sites, each of which is hosting spin-1 localized spin and with periodic boundary conditions so its first and last site are coupled by J_H in $\hat{H}_0$ in Eq. (32). For the clarity of notation, we use $\downarrow$, $\odot$, and $\uparrow$ to denote eigenstates of localized spin operator $\hat{S}_i^z$ with eigenvalues [Eq. (28c)] $m = -1$, $m = 0$, and $m = 1$, respectively. The one-magnon state is then given by

$$|q\rangle \equiv \frac{1}{\sqrt{N}}\sum_{n=0}^{N-1} e^{iqx_n}\,|\underbrace{\uparrow\cdots\uparrow}_{n\text{ times}}\odot\underbrace{\uparrow\cdots\uparrow}_{N-n-1\text{ times}}\rangle\,, \tag{52}$$

where $x_n = na_0$ is the real-space position of the localized spin on site $n+1$ and a_0 is the lattice spacing. The corresponding magnon energy-momentum dispersion is $\hbar\omega(q) = 2JS[1 - \cos(qa_0)]$.

The expectation value of the total z-spin operator of localized spins in state $|q\rangle$ is given by

$$\langle q|\sum_{i=1}^{N}\hat{S}_i^z\,|q\rangle = NS - 1, \tag{53}$$

which indicates that creation of a magnon with wave vector q removes one unit of total z spin from the ferromagnetic GS. *Because of this feature, presence of one HP boson or one HP magnon is labeled by the same* $N_{\rm mag} = 1$ *throughout the paper*. In addition, the expectation value of the localized z-spin operator at arbitrary site i,

$$\langle q|\,\hat{S}_i^z\,|q\rangle = S - \frac{1}{N}, \tag{54}$$

shows that excitation of one HP magnon reduces the z component of each localized spin by $1/N$. This rigorous quantum-mechanical result justifies the LLG picture [4] of

spin wave in which classical vectors of localized spins precess with frequency ω and with some small cone angle around the z axis, while the phase of the precession of adjacent vectors varies harmonically in space over wavelength λ.

In the second-quantization description produced by HP transformation, $|q\rangle = \hat{b}_q^\dagger|0\rangle$ is a *one-magnon Fock state* [97], where the creation operator of HP magnon is given by

$$\hat{b}_q^\dagger = \frac{1}{\sqrt{N}}\sum_{n=0}^{N-1} e^{ikx_n}\hat{a}_{n+1}^\dagger. \tag{55}$$

Note that such a one-magnon Fock state has been realized experimentally only very recently in a millimeter-sized ferrimagnetic crystal and detected by a superconducting qubit as the quantum sensor [97], thereby representing a counterpart in quantum magnonics of a single-photon detection from quantum optics.

It is worth mentioning that in spintronics and magnonics literature [48], one also finds $\hat{a}_i^\dagger|0\rangle$ denoted as one magnon created in real space at position i while $\hat{b}_q^\dagger|0\rangle$ is one magnon created in the reciprocal space with momentum $\hbar q$. However, the former is not an eigenstate of Hamiltonian in Eq. (51), while the latter is, so we differentiate between them by using HP boson for the former and HP magnon for the latter. As already highlighted, for both situations we use label $N_{\rm mag} = 1$ for simplicity of notation because in both cases one unit of the total z spin is removed from the ferromagnetic GS [Eq. (53)].

Nevertheless, we illustrate the distinction between HP bosons and HP magnons by initializing the $N = 7$ site chain [Fig. 1(a)] in the quantum state $|\Psi_1(0)\rangle = |\odot\uparrow\uparrow\uparrow\uparrow\uparrow\uparrow\rangle$ in Figs. 3(a) and 3(b) or in the quantum state $|\Psi_2(0)\rangle = |\downarrow\uparrow\uparrow\uparrow\uparrow\uparrow\uparrow\rangle$ in Figs. 3(c) and 3(d). This means that $N_{\rm mag} = 1$ HP boson is created on site $i = 1$ at $t = 0$ in the former case; while full spin flip of localized spin on site $i = 1$ in the latter case means that $N_{\rm mag} = 2$ HP bosons are created on site $i = 1$. Besides the pedagogical value, these initial states and the ensuing one- or two-magnon propagation including magnon bound states can be directly probed in experiments using ultracold atoms in an optical lattice where tracking the localized spin expectation values is possible with single-spin and single-site resolution [98].

Since $|\Psi_1(0)\rangle$ is not an eigenstate, it evolves in time to produce a spatiotemporal profile of the expectation value $\langle\hat{S}_i^z\rangle(t)$ [Fig. 3(a)] in the quantum state $|\Psi_1(t)\rangle$. For the quantum time evolution, we use the scheme explained in Sec. II H where interacting Hamiltonian $\hat{H}_{\rm lspins}$ from Eq. (5) is plugged in, but since only one HP boson is excited this is equivalent to using noninteracting $\hat{H}_0$ in Eq. (32). The "white trace" in Fig. 3(a) visualizes how HP boson moves from the left to the right edge of the chain while undergoing reflection on site $i = 7$ at $t \approx 2.5$ fs, as indicated by the horizontal dashed line, followed by multiple back-and-forth reflections. Note that since the 1D chain in Fig. 1(a) has open boundary conditions, its low-energy excited eigenstates differ [99] from textbook [8,9] HP magnons $|q\rangle$ in Eq. (52) as eigenstates of interacting localized spin systems with translational invariance. Figure 3(b) visualizes the overlap, $n_q(t) = |\langle q|\Psi_1(t)\rangle|^2$, between the many-body quantum state $|\Psi_1(t)\rangle$ with one HP boson and the one-magnon Fock state $|q\rangle$. Large values of $n_q(t)$ are observed in the region where $q > 0$ and $t \lesssim 2.5$ fs, coinciding

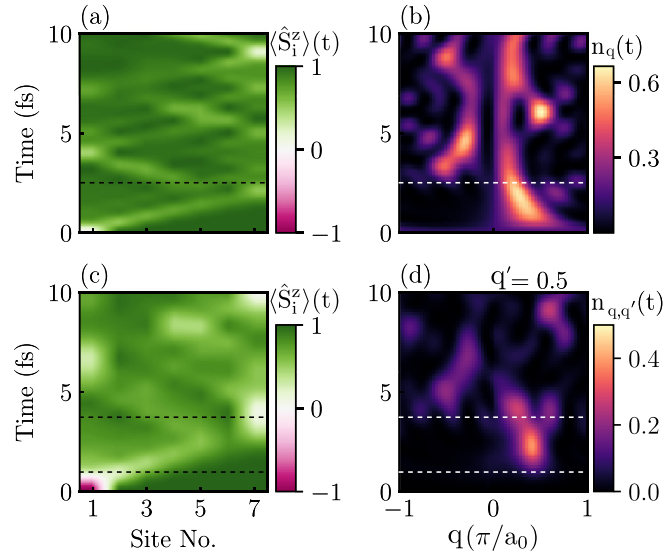

FIG. 3. (a) Spatiotemporal profile of the expectation value $\langle\hat{S}_i^z\rangle(t)$ across 1D spin chain in Fig. 1(a) composed of $N = 7$ sites hosting spin-1 localized spins where $N_{\rm mag} = 1$ HP boson is created at initial time $t = 0$ on site $i = 1$, such that $|\Psi_1(0)\rangle = |\odot\uparrow\uparrow\uparrow\uparrow\uparrow\uparrow\rangle$. (b) The corresponding probability, $n_q(t) = |\langle q|\Psi_1(t)\rangle|^2$, of finding quantum many-body state $|\Psi_1(t)\rangle$ at later times $t > 0$ in *one-magnon Fock state* $|q\rangle$ of momentum q as HP boson propagates from the left to right edge of the chain [white traces in (a)], thereby switching from $q > 0$ to $q < 0$ when reflection occurs near the boundary on site $i = 7$ and $t \gtrsim 2.5$ fs (indicated by dashed horizontal lines). (c) is counterpart of (a) when $N_{\rm mag} = 2$ HP bosons are created at $t = 0$ on site $i = 1$, such that $|\Psi_2(0)\rangle = |\downarrow\uparrow\uparrow\uparrow\uparrow\uparrow\uparrow\rangle$, with (d) showing the corresponding probability $n_{q,q'}(t) = |\langle q, q'|\Psi_2(t)\rangle|^2$ of finding quantum many-body state $|\Psi_2(t)\rangle$ at later times $t > 0$ in *two-magnon Fock state* $|q, q'\rangle$. Dashed horizontal lines in (d) mark times $t = 1$ fs and $t = 4$ fs. In all panels, we set $J_H = 1$ eV. For aesthetic purposes, in (a) and (c) we perform a cubic interpolation of the discrete data at $N = 1, 2, \cdots 7$ on the x axis that furnishes a continuous plot.

with the left-to-right motion of the HP boson in Fig. 3(a), which signifies excitation of $N_{\rm mag} = 1$ magnon with positive momentum. On the other hand, after reflection of the HP boson at the boundary (i.e., site $i = 7$) and $t \approx 2.5$ fs, a rapid rise of $n_q(t)$ in the $q < 0$ region is observed, which indicates excitation of $N_{\rm mag} = 1$ magnon with negative momentum. This is consistent with the intuitive picture of HP boson reflecting back-and-forth between the hard walls of our 1D chain with open boundary conditions.

The Fock states of $N_{\rm mag} = 2$ magnons carrying momentum $\hbar q$ and $\hbar q'$ are defined by [100]

$$|q, q'\rangle = \sum_{n>m} f_{mn}(q, q')\,|\underbrace{\uparrow\cdots\uparrow}_{m-1\text{ times}}\odot\uparrow\cdots\uparrow\odot\underbrace{\uparrow\cdots\uparrow}_{N-n\text{ times}}\rangle, \tag{56}$$

where

$$f_{mn}(q, q') = \frac{1}{\mathcal{N}}[e^{iqx_m}e^{iq'x_n} + e^{iq'x_n}e^{iqx_m}]. \tag{57}$$

Here $\mathcal{N}$ is the normalization constant and $f_{mn}(q, q')$ is symmetric under exchange $q \leftrightarrow q'$ ensuring $|q, q'\rangle = |q', q\rangle$ to satisfy the symmetrization postulate of quantum mechanics for bosonic particles—as manifestly encoded

by second-quantization formalism, $|q,q'\rangle = \hat{b}^\dagger_q \hat{b}^\dagger_{q'} |0\rangle = \hat{b}^\dagger_{q'} \hat{b}^\dagger_q |0\rangle = |q',q\rangle$.

Figure 3(c) plots the spatiotemporal profile of $\langle \hat{S}^z_i \rangle(t)$ in quantum state $|\Psi_2(t)\rangle$ starting from $|\Psi_2(0)\rangle = |\downarrow\uparrow\uparrow\uparrow\uparrow\uparrow\uparrow\uparrow\rangle$. For quantum time evolution, we use the scheme explained in Sec. II H where interacting Hamiltonian $\hat{H}_{\text{lspins}}$ from Eq. (5) is plugged in, so two HP bosons are correlated by (i) bosonic statistics and (ii) interactions in $\hat{H}_{\text{int}}$ [Eq. (33)], where $N_T \to \infty$. The two HP bosons propagate immediately from the left to the right for $t > 0$, as shown by white traces in Fig. 3(c). The corresponding overlap, $n_{q,q'}(t) = |\langle q,q'|\Psi_2(t)\rangle|^2$, in Fig. 3(d) is $n_{q,q'}(t) = 0$ for $t \lesssim 1$ fs, which is explained by Eq. (56) where the two-magnon Fock state is composed of terms containing two HP bosons on different sites $m \neq n$. Since at $t = 0$ the two HP bosons are on the same site $i = 1$, we find $n_{q,q'}(t = 0) = 0$. However, this holds until $t \lesssim 1$ fs (indicated by horizontal dashed line), after which the two HP bosons are physically separated in real space, as confirmed by the emergence of nonzero values of $n_{q,q'}(t)$ thereafter. We also note that for $1 \lesssim t \lesssim 4$ fs (indicated by horizontal dashed line), the region near $q = 0.5\ \pi/a_0$ shows large values of $n_{q,q'}(t)$, and since $q' = 0.5\,\pi/a_0$ is fixed for all values of q in Fig. 3(d), we can conclude that two HP bosons possess nearly the same velocity. Beyond $t \approx 4$ fs, nonzero values of $n_{q,q'}(t)$ in the region with $q < 0$ and $q > 0$ coexist, which indicates that one HP boson moves toward the right while the other moves toward the left edge of the chain.

J. Retarded and lesser one-particle Green's functions

The fundamental quantities of nonequilibrium GF formalism [24,25] for fermions are the one-particle retarded GFs,

$$G^r_{i\sigma,j\sigma'}(t,t') = -i\hbar^{-1}\Theta(t-t')\,\langle\{\hat{c}_{i\sigma}(t), \hat{c}^\dagger_{j\sigma'}(t')\}\rangle\,, \tag{58}$$

and the one-particle lesser GF,

$$G^<_{i\sigma,j\sigma'}(t,t') = i\hbar^{-1}\,\langle \hat{c}^\dagger_{j\sigma'}(t')\hat{c}_{i\sigma}(t)\rangle\,, \tag{59}$$

which describe the density of available quantum states and how electrons occupy those states, respectively. Here $\Theta(t-t')$ is the Heaviside function, $\hat{c}_{i\sigma}(t)$ indicates Heisenberg picture time evolution of $\hat{c}_{i\sigma}$, and $\langle\cdots\rangle = \text{Tr}(\hat{\rho}\cdots)$ is the quantum statistical average, where $\hat{\rho}$ is the density operator of the system at $t = 0$. Analogously, the bosonic one-particle retarded GF is defined by

$$D^r_{ij}(t,t') = -i\hbar^{-1}\Theta(t-t')\,\langle[\hat{a}_i(t), \hat{a}^\dagger_j(t')]\rangle\,, \tag{60}$$

and the lesser GF is defined by

$$D^<_{ij}(t,t') = -i\hbar^{-1}\,\langle \hat{a}^\dagger_j(t')\hat{a}_i(t)\rangle\,. \tag{61}$$

In equilibrium or in steady-state nonequilibrium, these GFs depend solely on $\tau = t - t'$ and can be Fourier transformed to energy domain [38], such as

$$G^{r,<}_{i\sigma,j\sigma'}(E) = \int_{-\infty}^{+\infty} d\tau\, G^{r,<}_{i\sigma,j\sigma'}(\tau) e^{iE\tau/\hbar}, \tag{62}$$

for electrons and

$$D^{r,<}_{ij}(E) = \int_{-\infty}^{+\infty} d\tau D^{r,<}_{ij}(\tau) e^{iE\tau/\hbar}, \tag{63}$$

for bosons. We emphasize that the very definition of GFs for the localized spin subsystem, i.e., magnons, in Eqs. (60) and (61) *requires* us to use bosonic operators. Therefore, when exactly evaluating these GFs in Secs. III E and III G, we numerically compute the square root of the bosonic operators in Eqs. (1).

K. Spectral function for electrons and magnons

The electronic spectral function $A(E)$, or the interacting density of states [85,86], is computed using the retarded GF in Eq. (62) as

$$\begin{aligned} A(E) &= -2\sum_{i=1}^{N}\sum_{\sigma=\uparrow,\downarrow} \text{Img}\big[G^r_{i\sigma,i\sigma}(E)\big] \\ &= \sum_k W^+_k \delta(E-\Delta_k) + W^-_k \delta(E+\Delta_k), \end{aligned} \tag{64}$$

where $\Delta_k = (E_k - E_0)$ and E_k are the eigenenergies of quantum many-body Hamiltonian $\hat{H}$ [Eq. (4)]. The prefactors of the δ function in $A(E)$,

$$W^+_k = \sum_{i=1}^{N}\sum_{\sigma=\uparrow,\downarrow} |\langle\Psi_k|\hat{c}^\dagger_{i\sigma}|\Psi_0\rangle|^2, \tag{65a}$$

$$W^-_k = \sum_{i=1}^{N}\sum_{\sigma=\uparrow,\downarrow} |\langle\Psi_k|\,\hat{c}_{i\sigma}\,|\Psi_0\rangle|^2, \tag{65b}$$

define the weight of the many-body eigenstate $|\Psi_k\rangle$ within $A(E)$. Since the GS $|\Psi_0\rangle$ is an eigenstate of the electron number operator $\hat{N}_e$ [Eq. (18)], it has a well-defined number of electrons N_e. Thus, the action of $\hat{c}^\dagger_{i\sigma}$ and $\hat{c}_{i\sigma}$ on $|\Psi_0\rangle$ in Eq. (65) reveals that the δ function peaks at $E = \pm\Delta_k$ can only be contributed by those quantum many-body eigenstates $|\Psi_k\rangle$ which describe systems containing $N_e \pm 1$ electrons.

Similarly, the bosonic spectral function $D(E)$ is evaluated using the bosonic retarded GF in Eq. (63),

$$\begin{aligned} D(E) &= -2\sum_{i=1}^{N} \text{Img}\big[D^r_{ii}(E)\big] \\ &= \sum_k Q^+_k \delta(E-\Delta_k) - Q^-_k \delta(E+\Delta_k), \end{aligned} \tag{66}$$

where

$$Q^+_k = \sum_i |\langle\Psi_k|\,\hat{a}^\dagger_i\,|\Psi_0\rangle|^2, \tag{67a}$$

$$Q^-_k = \sum_i |\langle\Psi_k|\,\hat{a}_i\,|\Psi_0\rangle|^2, \tag{67b}$$

define the weight of many-body eigenstate $|\Psi_k\rangle$ within $D(E)$. The δ-function peaks in Eq. (66) at $E = \pm\Delta_k$ come from many-body eigenstates $|\Psi_k\rangle$. However, unlike the electronic case, they do not have a well-defined total magnon number N_{mag} as they are not eigenstates of the total magnon number operator $\hat{N}_{\text{mag}} = \sum_{i=1}^{N} \hat{n}_i$. This is illustrated by Fig. 9(e) with the structure of one selected many-body eigenstate $|\Psi_k\rangle$, which is a linear combination of many-body states with total magnon number $N_{\text{mag}} = 0$, $N_{\text{mag}} = 1$, and $N_{\text{mag}} = 2$.

Both $A(E)$ and $D(E)$ must satisfy the *sum rule*

$$\int_{-\infty}^{+\infty} \frac{dE}{2\pi} A(E) = 2N, \tag{68a}$$

$$\int_{-\infty}^{+\infty} \frac{dE}{2\pi} D(E) = N. \tag{68b}$$

This feature allows for physical interpretation where $A(E)dE/2N$ or $D(E)dE/N$ can be viewed as probabilities to find a fermion or boson, respectively, within energy window dE around E in a general quantum many-body system where fermions interact with other fermions and bosons interact with other bosons, as well as with each other. Note that our fermion-boson interacting system, as illustrated in Fig. 1(b) and described by the Hamiltonian in Eq. (4), includes HP bosons interacting [Eq. (33)] with other HP bosons when $N_{\rm mag} > 1$ and electrons interacting with HP bosons while electron-electron interactions are excluded. Since the sum rule is an exact result, in practical GF calculations it can be employed to test the quality of a variety of analytical and numerical approximations [38].

III. RESULTS AND DISCUSSION

A. Range of validity of truncated HP transformation for nonequilibrium interacting system of magnons

Figure 4 compares $\langle \hat{S}_1^z \rangle(t)$ for a 1D chain [Fig. 1(a)], hosting $S = 5/2$ or $S = 1$ localized spins in the absence of electrons (i.e., $N_e = 0$), computed using the original localized spin operators versus their mapping to bosonic operators via the truncated HP transformation. In the ferromagnetic GS $|\Psi_0\rangle$, the expectation value $\langle \hat{S}_i^z \rangle(t=0) = \langle \Psi_0 | \hat{S}_i^z | \Psi_0 \rangle = 5/2$ for all sites i at $t = 0$ in Figs. 4(a)–4(c). To initiate nonequilibrium dynamics for times $t > 0$, we choose an initial state $|\Psi(0)\rangle$ such that the expectation value of the localized spin on site $i = 1$ is reduced by $N_{\rm mag}$ units, $\langle \hat{S}_{i=1}^z \rangle(t=0) = \langle \Psi(0) | \hat{S}_{i=1}^z | \Psi(0) \rangle = (5/2 - N_{\rm mag})$, while on other sites it remains $S_{i\neq 1}^z(t=0) = 5/2$. This is equivalent to introducing $N_{\rm mag}$ HP bosons on site $i = 1$ at $t = 0$, so the initial quantum many-body state of HP bosons is given by

$$|\Psi(0)\rangle = (\hat{a}_1^\dagger)^{N_{\rm mag}} |0\rangle . \tag{69}$$

When $N_{\rm mag} = 1$, Fig. 4(a) shows that $\langle \hat{S}_1^z \rangle(t)$, evaluated by truncated HP transformation (green dashed line) solely containing single-particle Hamiltonian $\hat{H}_0$ of noninteracting HP bosons in Eq. (32), accurately tracks the exact time dependence (black lines) of $S_1^z(t)$ evaluated using the localized spin operators. This feature is trivially expected because there is only *one* HP boson in the system and magnon-magnon interaction terms active within $\hat{H}_{\rm int}$ part of the Hamiltonian [Eq. (33)] cannot influence the dynamics of localized spins.

To understand the significance of magnon-magnon interaction terms within $\hat{H}_{\rm int}$ on the dynamics of localized spins, we next introduce $N_{\rm mag} = 2$ HP bosons on site $i = 1$. The time dependence of $\langle \hat{S}_1^z \rangle(t)$ in Fig. 4(b), evaluated via the truncated HP transformation with truncation number $N_T = 1$ (Sec. II E), matches the exact time evolution obtained using the original localized spin operators only for short enough times ($0 < t < 10$ fs). At longer times ($30 < t < 35$ fs), discrepancy emerges due to missing effects from $N_T > 1$ magnon-magnon interaction terms within $\hat{H}_{\rm int}$. Thus, to recover the agreement between two types of calculations at longer times requires increasing N_T, such as by using $N_T = 3$ (orange dashed lines) in Fig. 4(b). However, progressively larger N_T must be employed (Fig. 5) to increase the breakdown time $t_{\rm break}$ [marked in Figs. 4(d) and 4(e)] at which disagreement between two types of calculations emerges. We define $t_{\rm break}$ as the time when the deviation $\Delta = \langle \hat{S}_1^z \rangle(t)|_{\rm HP} - \langle \hat{S}_1^z \rangle(t)|_{\rm exact}$, between $\langle \hat{S}_1^z \rangle(t)|_{\rm HP}$ (evaluated from truncated HP transformation with a truncation number N_T) and the exact $\langle \hat{S}_1^z \rangle(t)|_{\rm exact}$ becomes larger than the chosen tolerance $|\Delta| > 10^{-4}$.

As demonstrated by Figs. 4(d), 4(e), and 5, $t_{\rm break}$ sensitively depends on the density of HP bosons, $N_{\rm mag}/N$, whose increase makes magnon-magnon interaction terms within $\hat{H}_{\rm int}$ more relevant, thereby requiring larger N_T in Fig. 5. Figures 4(d) and 4(e) corroborate this conclusion by showing the effect of reduced density of HP bosons on the range of validity of truncated HP transformation, where we employ spin-1 localized spins allowing us to exactly diagonalize larger chains [than those composed of $N = 4$ sites in Fig. 4(a)–4(c) with spin-$\frac{5}{2}$ on each site]. In Fig. 4(d), at $t = 0$ we flip the localized spins on sites $i = 1$ and $i = 2$ [see inset in Fig. 4(d)], thereby introducing two HP bosons on each of these sites. Thus, the total number of HP bosons within the system in Fig. 4(d) is $N_{\rm mag} = 4$, whereas the HP boson density is $N_{\rm mag}/N = 1$. For such parameters, $t_{\rm break} \approx 11$ fs ($|\Delta| = 0.05$ is chosen solely for visualization of $t_{\rm break}$ at fs timescales). On the other hand, in Fig. 4(e), where HP boson density is reduced to $N_{\rm mag}/N = 0.57$ by making the 1D chain longer from $N = 4$ sites to $N = 7$ sites, we find that $t_{\rm break}$ for truncated HP transformation increases to $t_{\rm break} \approx 23$ fs. This observation is easily explained since in longer 1D chains the probability for magnon-magnon scattering events is reduced, which makes inclusion of high-order magnon-magnon interaction terms less important and thus the breakdown time for truncated HP transformation increases.

Figure 5 demonstrates how for a given breakdown time $t = t_{\rm break}$, the horizontal distance between consecutive curves from left to right increases nonlinearly. This means that N_T needed to accurately track $\langle \hat{S}_1^z \rangle(t)$ via the truncated HP transformation increases nonlinearly with the number of HP bosons $N_{\rm mag}$ excited in the system. On the other hand, if we consider the roughly constant slope p of each curve in Fig. 5 (for the part before a sudden jump) and note the logarithmic scale for the ordinate axis of Fig. 5, we can conclude that $t_{\rm break} \propto \exp(pN_T)$. At first sight, the exponential dependence of $t_{\rm break}$ on N_T appears to be favorable, i.e., by using larger values of N_T (and hence including more and more multimagnon terms), we can increase $t_{\rm break}$ exponentially and yield accurate dynamics for longer times. However, to obtain a practically tractable MBPT for electron-boson interacting systems [101], a small N_T is required, but Fig. 5 shows that using small N_T = 1-5 allows one to track dynamics of localized spins only up to time $t_{\rm break} \approx 1.5\hbar/J_H \approx 15.0$ fs (for $J_H = 0.1$ eV). This is insufficient to model even ultrafast optical manipulation of magnetism requiring simulation times ∼10 fs [102] and it is much further away from current-driven magnetization dynamics via spin torque which occurs on ∼1 ns timescales [51,53].

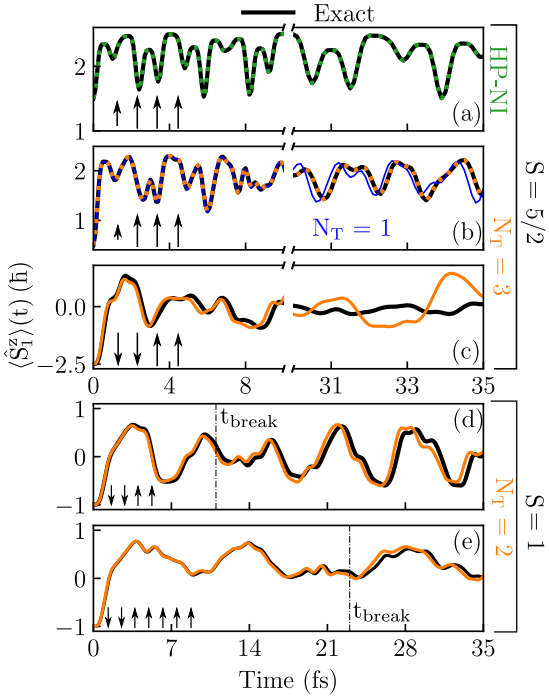

FIG. 4. Comparison of the *exact* time-dependence $\langle \hat{S}_i^z \rangle (t)$ (black lines) obtained by using localized spin operators versus *approximative* time dependence obtained by using truncated HP transformation [Sec. II E], with a truncation number N_T, for 1D quantum spin chain in Fig. 1(a). The chain is composed of $N = 4$ sites hosting spin-$\frac{5}{2}$ [(a)–(c)] or spin-1 [(d)–(e)] localized spins. At $t = 0$, $N_{\rm mag}$ HP bosons are created on site $i = 1$ or both sites $i = 1$ and $i = 2$, as illustrated by the reduced size of arrows or their full reversal in the inset at the lower left corner within each panel (see Sec. II G for proper association of quantum states to illustration in the insets). In (a), $N_{\rm mag} = 1$ so $\langle \hat{S}_i^z \rangle (t)$ evaluated (green dotted line) from noninteracting (NI) HP boson Hamiltonian [Eq. (32)] is identical to the exact $\langle \hat{S}_i^z \rangle (t)$. In (b), $N_{\rm mag} = 2$ and $\langle \hat{S}_i^z \rangle (t)$ evaluated from truncated HP transformation with $N_T = 1$ (blue line) disagrees with the exact $\langle \hat{S}_i^z \rangle (t)$, but increasing to $N_T = 3$ (orange dotted line) matches the exact result. Nevertheless, in (c), creation of $N_{\rm mag} = 10$ HP magnons, by full reversal of two localized spins while keeping $N_T = 3$, leads to disagreement between truncated HP transformation (orange line) and exact (black line) results for $\langle \hat{S}_i^z \rangle (t)$. In (d) and (e), we use chains of $N = 4$ and 7 sites, respectively, where orange lines indicate $\langle \hat{S}_i^z \rangle (t)$ computed from truncated HP transformation with $N_T = 2$. The vertical dot-dash lines in (d) and (e) explicitly mark breakdown time $t = t_{\rm break}$ (see also Fig. 5) at which truncated HP transformation starts to deviate from the exact result for $\langle \hat{S}_i^z \rangle (t)$. In all panels, we set $J_H = 1$ eV.

B. Range of validity of truncated HP transformation for nonequilibrium interacting system of electrons and magnons

In this section, we repeat the same analysis as in Sec. III A—but with electron–localized-spin or, equivalently, electron-magnon—interaction turned on within 1D quantum many-body system composed of $N = 3$ sites [Fig. 1(b)]. These sites host spin-$\frac{5}{2}$ localized spins interacting with half-filled ($N_e = 3$) tight-binding electrons via the *sd* exchange interaction [71] of strength $J_{\rm sd}$ as encoded by Eq. (9).

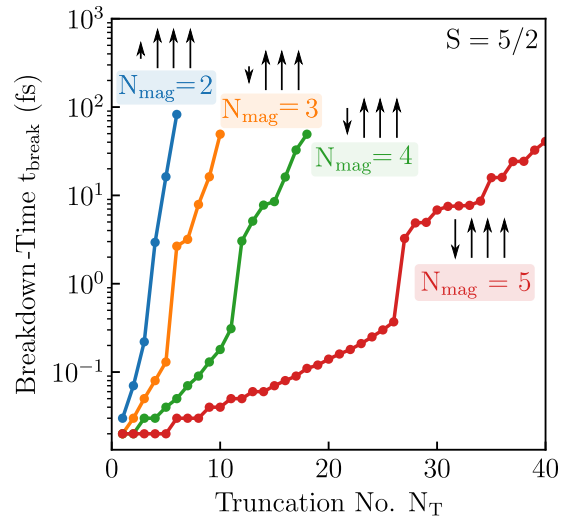

FIG. 5. Breakdown time $t_{\rm break}$, as the time at which truncated HP transformation starts to deviate [see Figs. 4(d) and 4(e)] from the exact result for $\langle \hat{S}_1^z \rangle (t)$, as function of truncation number N_T. The inset near each line indicates the number of HP bosons $N_{\rm mag}$ created at $t = 0$ within 1D quantum spin chain [Fig. 1(a)] composed of $N = 4$ sites hosting spin-$\frac{5}{2}$ localized spins interacting via Heisenberg exchange $J_H = 1$ eV.

At $t = 0$, we fully flip the localized spin-$\frac{5}{2}$ on site $i = 1$ to initiate nonequilibrium dynamics. From the viewpoint of HP transformation, this is equivalent to introducing $N_{\rm mag} = 5$ HP bosons on site $i = 1$ and, thus, the initial quantum many-body state is given by

$$|\Psi(0)\rangle = (\hat{a}_1^\dagger)^5 \hat{c}_{2\uparrow}^\dagger \hat{c}_{1\uparrow}^\dagger \hat{c}_{1\downarrow}^\dagger |0\rangle \tag{70}$$

in the notation of second-quantization formalism. Here $|0\rangle$ is the vacuum state of electrons and HP bosons combined. Figure 6(a) with $J_{\rm sd} = 0$ serves as a reference. When the electron-magnon interaction is turned on ($J_{\rm sd} = 1$ eV) in Fig. 6(b), $\langle \hat{S}_1^z \rangle (t)$ computed by truncated HP transformation follows the exact result for longer times $t \lesssim 15$ fs than in Fig. 6(a). This is explained by Fig. 6(c), which shows that the total number of magnons as a function of time, $N_{\rm mag}(t) = \sum_{i=1}^N \langle \Psi(t)| \hat{n}_i |\Psi(t)\rangle$, is reduced in the course of quantum time evolution. Therefore, this leads to fewer magnon-magnon scattering events, which facilitates accurate tracking over longer time intervals of nonequilibrium dynamics of localized spins by truncated HP transformation, in accord with Fig. 5. The lost magnons in Fig. 6(c) are absorbed by the electronic subsystem and mediate transfer of spin angular momentum between the subsystems of electrons and localized spins, while the total z spin remains conserved [Eq. (21)].

Furthermore, Figs. 6(d) and 6(e), as the counterpart of Figs. 6(a) and 6(b), respectively, demonstrate that electron-boson interacting Hamiltonian can track exact time evolution if truncated HP transformation is replaced by resummed HP transformation in Eq. (37). That is, when $N_{\rm max} = 3$ is used in Eq. (37), there is disagreement between the two calculations of $\langle \hat{S}_1^z \rangle (t)$—compare resummed HP transformation (magenta solid line) versus the exact one (black solid line)

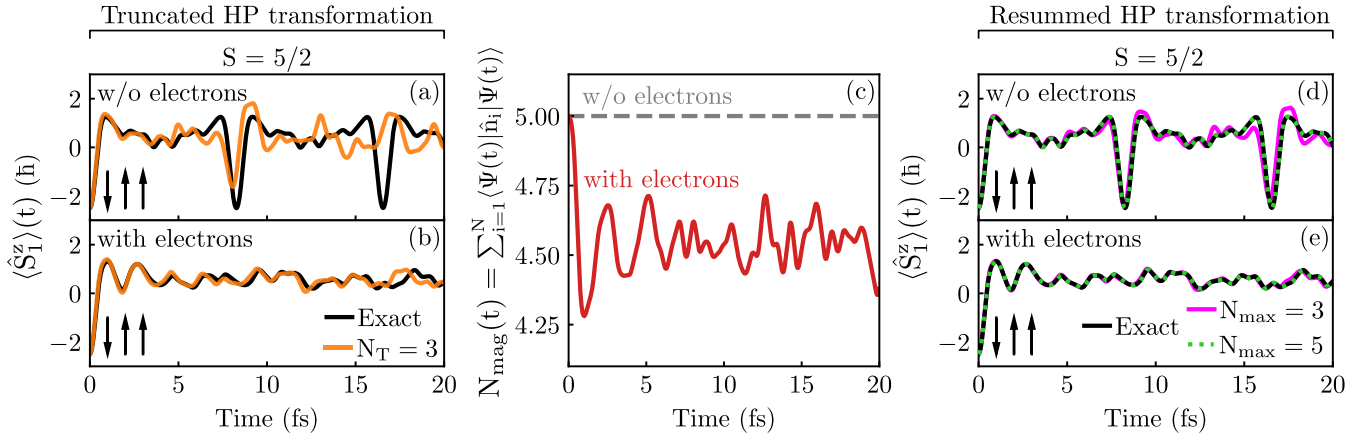

FIG. 6. (a) Comparison of the *exact* time dependence $\langle \hat{S}_i^z \rangle (t)$ (black line) evaluated using localized spin operators versus time dependence computed from truncated HP transformation (Sec. II E), with a truncation number N_T (orange line), for 1D quantum many-body system [Fig. 1(b)] comprised of $N = 3$ sites hosting spin-$\frac{5}{2}$ localized spins which interact with conduction electrons. The electron–localized-spin *sd* exchange interaction is turned off ($J_{sd} = 0$) in (a) for reference, and turned on in (b), using $J_{sd} = 1$ eV. The insets in both panels depict the state of localized spins at $t = 0$, where the localized spin on site $i = 1$ is completely reversed [i.e., $N_{mag} = 5$ HP bosons are created on site $i = 1$ via Eq. (70)] to initiate nonequilibrium dynamics. When *sd* interaction is turned on, the disagreement between two types of calculations is actually alleviated when moving from (a) to (b), which is explained by (c) as being due to a rapid loss of total number of magnons, $N_{mag}(t) = \sum_{i=1}^{N} \langle \Psi(t)| \hat{n}_i |\Psi(t)\rangle$, from the localized spin subsystem to the electronic subsystem. (d) and (e) are counterparts of (a) and (b), respectively, for $\langle \hat{S}_i^z \rangle (t)$ evaluated using the resummed HP transformation in Eq. (37), which is *approximate* for $N_{max} = 3$ but it becomes *exact* for $N_{max} = 2S = 5$.

but increasing $N_{max} = 5$ [which produces green dotted line in Fig. 6(e)] in Eq. (37) ensures that both calculations match perfectly.

Thus, Figs. 6(d) and 6(e) with properly chosen N_{max} motivate us to derive the following electron-boson Hamiltonian:

$$\hat{H} = \hat{H}_e + \hat{H}_{mag} + \hat{H}_{mag-mag} + \hat{H}_{e-mag} \tag{71}$$

as the *exact* mapping of the original electron–localized-spin Hamiltonian in Eq. (4). The former is required for equilibrium or nonequilibrium MBPT [24,25] which can handle [38] systems in two or three dimensions composed of a large number of sites $N \gg 1$. These are the problems where exact diagonalization [69], suitable for a small number of sites N, or (time-dependent) density matrix renormalization group [103–106], suitable for $N \gg 1$ but only in quasi-1D [107], are inapplicable. Here the terms in Eq. (71) are given by

$$\hat{H}_e = -\gamma \sum_{\langle ij \rangle} \hat{\psi}_i^\dagger \hat{\psi}_j, \tag{72a}$$

$$\hat{H}_{mag} = 2SJ_H \sum_{i=1}^{N} \hat{a}_i^\dagger \hat{a}_i - J_H S \sum_{\langle ij \rangle} (\hat{a}_i^\dagger \hat{a}_j + \hat{a}_j^\dagger \hat{a}_i), \tag{72b}$$

$$\hat{H}_{mag-mag} = -J_H \sum_{\langle ij \rangle} (\hat{a}_i^\dagger \hat{a}_i)(\hat{a}_j^\dagger \hat{a}_j) - J_H S \sum_{\langle ij \rangle} \sum_{n=0}^{N_{max}} \sum_{m=0}^{N_{max}} Q_n Q_m (1 - \delta_{n0}\delta_{m0}) \left[(\hat{a}_i^\dagger)^n \hat{a}_i^{n+1} (\hat{a}_j^\dagger)^{m+1} \hat{a}_j^m + (\hat{a}_i^\dagger)^{n+1} \hat{a}_i^n (\hat{a}_j^\dagger)^m \hat{a}_j^{m+1} \right], \tag{72c}$$

$$\hat{H}_{e-mag} = \sqrt{2} S J_{sd} \sum_{i=1}^{N} \sum_{n=0}^{N_{max}} Q_n \left[\hat{\psi}_{i\uparrow}^\dagger \hat{\psi}_{i\downarrow} (\hat{a}_i^\dagger)^{n+1} \hat{a}_i^n + \hat{\psi}_{i\downarrow}^\dagger \hat{\psi}_{i\uparrow} (\hat{a}_i^\dagger)^n \hat{a}_i^{n+1} \right]. \tag{72d}$$

Their physical meaning is transparent: $\hat{H}_e$ is the tight-binding Hamiltonian of noninteracting electrons, $\hat{H}_{mag}$ is the Hamiltonian of noninteracting HP bosons, $\hat{H}_{mag-mag}$ describes various interactions between two (first term in $\hat{H}_{mag-mag}$) or more HP bosons, and $\hat{H}_{e-mag}$ describes electron-boson interactions, such as absorption or emission of HP bosons accompanied by electron spin flip as the spin angular momentum is transferred. We note that Eq. (72) is much more complex than what is typically used in spintronics literature [38,41,44–46,48]. Most importantly, it shows that accurate MBPT or diagrammatic Monte Carlo calculations [108,109] in the future for interacting electron-magnon systems will have to deal with nonlinear [101] electron-boson interactions.

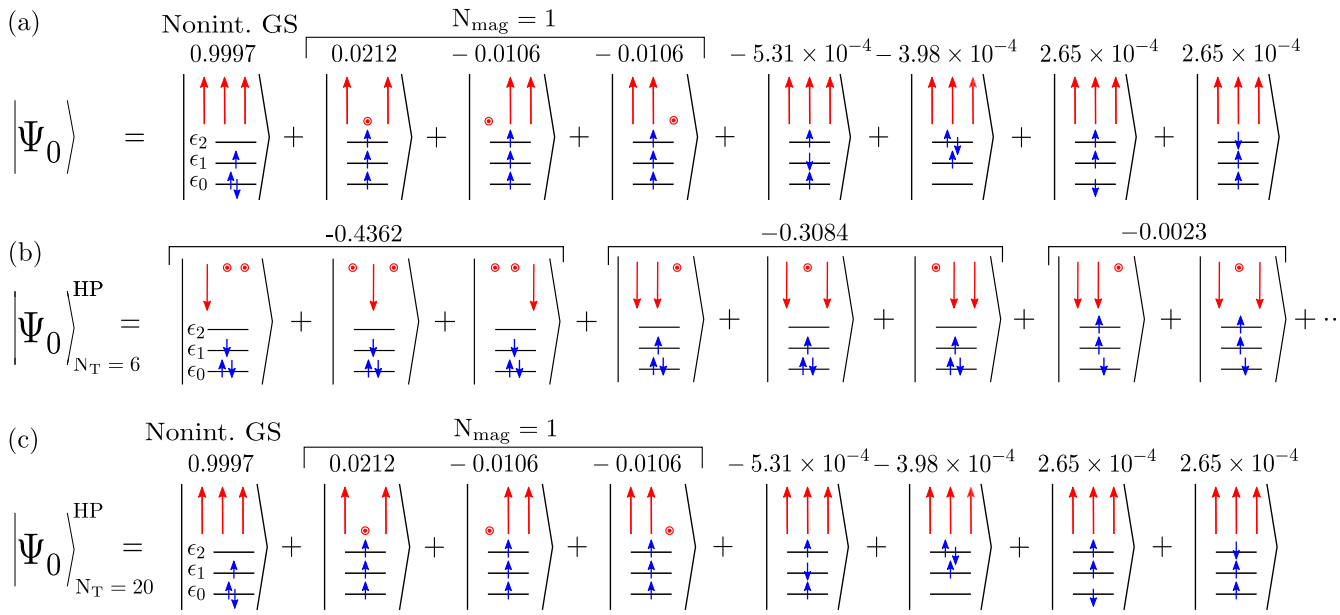

FIG. 7. (a) Composition of the *exact* GS $|\Psi_0\rangle$ of 1D quantum many-body system, illustrated in Fig. 1(b) and composed of $N = 3$ sites hosting spin-1 localized spins, which is computed by exact diagonalization of Hamiltonian in Eq. (4) expressed in terms of localized spin operators. In every ket in the sum, red arrows depict localized spins, whereas blue arrows indicate spin states of $N_e = 3$ electrons distributed among eigenenergy levels $\epsilon_0 = -\sqrt{2}\,\text{eV}$, $\epsilon_1 = 0\,\text{eV}$, and $\epsilon_2 = \sqrt{2}\,\text{eV}$ of noninteracting single-particle electronic Hamiltonian in Eq. (13). (b) The composition of *approximate* GS evaluated by exact diagonalization of Hamiltonian in Eq. (4) whose localized spins are mapped to bosonic operators via the truncated HP transformation (Sec. II E) with truncation number $N_T = 6$. (c) shows that to match the composition of the exact GS from (a) requires to increase $N_T = 20$ in truncated HP transformation. Numbers on the top of each ket are coefficients in their linear superpositions comprising the respective GS. In all panels, we set $J_H = J_{sd} = 0.2\,\text{eV}$. Note that the first ket in (a) and (c) is noninteracting GS for a system where electrons and localized spins are decoupled by using $J_{sd} = 0$.

C. Ground state of interacting system of electrons and magnons

The exact GS is obtained in three steps: (i) $\hat{H}$ is represented as a matrix in the basis of eigenstates of $\hat{N}_e$ and $\hat{S}^z_{tot}$ to render a block-diagonal matrix as shown in Fig. 2(c); (ii) to ensure half-filling for electrons, the matrix block corresponding to $N_e = 3$ electrons is isolated; and (iii) this matrix block is diagonalized and the eigenstate with the lowest eigenenergy E_0 is identified as the GS. Obviously, if in step (i) $\hat{H}$ is expressed directly in terms of localized spin operators [Eqs. (28)], then step (iii) yields the *numerically exact* GS, $|\Psi_0\rangle$. On the other hand, if $\hat{H}$ is expressed using the truncated HP transformation with a truncation number N_T [Eq. (31)], then thus obtained GS $|\Psi_0\rangle^{HP}_{N_T}$ is not guaranteed to be the same as $|\Psi_0\rangle$. In this section, we examine the structure of $|\Psi_0\rangle$ and identify the value of N_T required to ensure that $|\Psi_0\rangle^{HP}_{N_T} = |\Psi_0\rangle$.

Figure 7(a) depicts the numerically exact GS $|\Psi_0\rangle$ as a linear combination [93] of many-body kets where red arrows denote quantum state of localized spins (using the same notation as introduced in Sec. III I for spin-1 localized spins) while blue arrows denote spin-↑ or spin-↓ electrons filling three single-particle energy levels $\epsilon_0 = -\sqrt{2}\,\text{eV}$, $\epsilon_1 = 0$, and $\epsilon_2 = \sqrt{2}\,\text{eV}$ of noninteracting tight-binding Hamiltonian $\hat{H}_e$ [Eq. (8)]. In contrast, we find in Fig. 7(b) that GS $|\Psi_0\rangle^{HP}_{N_T=6}$ evaluated using truncated HP transformation with $N_T = 6$ is entirely different from $|\Psi_0\rangle$ shown in Fig. 7(a). Only when the truncation number is increased to $N_T = 20$ in Fig. 7(c), we find $|\Psi_0\rangle^{HP}_{N_T=20} \equiv |\Psi_0\rangle$.

It is worth examining further the structure of the exact GS $|\Psi_0\rangle$ in Fig. 7(a). Its many-body eigenenergy is $E_0 = -3.33\,\text{eV}$ while the other quantum numbers [Eq. (22)] are $N_e = 3$ and $S^z_{tot} = 3.5$. The largest contribution (greater than 99%) to $|\Psi_0\rangle$ comes from the first term on the RHS in Fig. 7(a) where $N_e = 3$ electrons fill up the single-particle energy levels ϵ_0, ϵ_1, and ϵ_2 of noninteracting Hamiltonian $\hat{H}_e$ [Eq. (8)] in accord with the Pauli exclusion principle while the localized spins are in the ferromagnetic configuration. In the absence of electron–localized-spin interaction, the first term on the RHS would be the only nonzero one. Thus, interactions give rise to three states [indicated by horizontal overline in Fig. 7(a)], where $N_{mag} = 1$ HP boson is created on one of the three sites. This HP boson is actually emitted when the spin-↓ electron in eigenenergy level ϵ_0 undergoes a spin-flip process and emerges as a spin-↑ electron in eigenenergy level ϵ_2. This process respects conservation of total z spin encoded by Eq. (21). The remaining four kets on the RHS of Fig. 7(a) are purely electronic excitations where electrons are excited among eigenenergy levels ϵ_0, ϵ_1, and ϵ_2 but are not accompanied by any spin-flips of localized spins.

D. Electronic spectral function in interacting system of electrons and magnons

For the same system considered in Sec. III C, Figs. 8(a)–8(c) compare the electronic spectral function $A(E)$ [Eq. (64)] evaluated from truncated HP transformation versus the

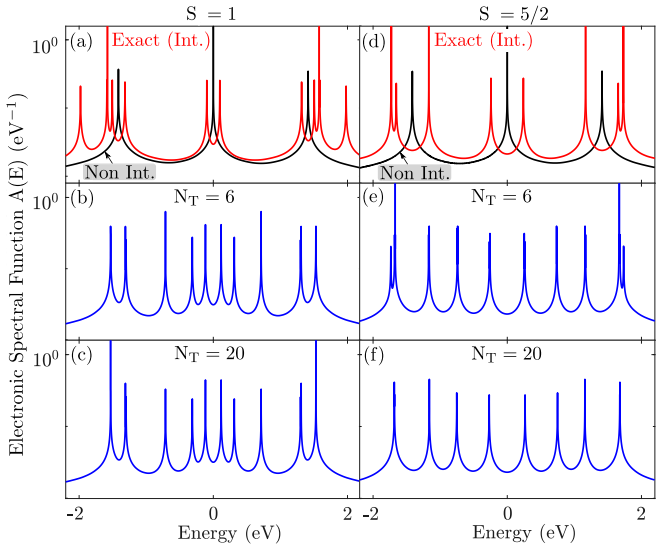

FIG. 8. (a) The *exact* electronic spectral function $A(E)$ (red lines) in Eq. (64) for 1D quantum many-body system, illustrated in Fig. 1(b) and comprised of $N = 3$ sites hosting spin-1 localized spins, is evaluated using localized spin operators in Hamiltonian in Eq. (4). This is compared to *approximate* $A(E)$ in (b) and (c) evaluated by mapping localized spin operators to bosonic operators via truncated HP transformation (Sec. II E) with truncation numbers $N_T = 6$ and $N_T = 20$, respectively. (d)–(f) show counterpart information to (a)–(c) but for spin-$\frac{5}{2}$ localized spins on each of $N = 3$ sites. In all panels, we set $J_H = J_{sd} = 0.2\,\text{eV}$, except for black curves in (a) and (d) for which electron–localized-spin interaction is turned off, i.e., $J_{sd} = 0$.

exact one evaluated using localized spin operators. To set a reference point, in Fig. 8(a) we first consider the noninteracting electronic spectral function (black line) when electron–localized-spin interaction is turned off ($J_{sd} = 0$). For such a case, the available single-particle states are simply the eigenstates of the noninteracting tight-binding Hamiltonian $\hat{H}_e$ [Eq. (8)] with single-particle energy levels ϵ_0, ϵ_1, and ϵ_2, so $A(E)$ consists of sharp peaks centered at ϵ_0, ϵ_1, and ϵ_2. Upon turning on electron–localized-spin interaction ($J_{sd} = 0.2\,\text{eV}$), the exact $A(E)$ (red line) evaluated using localized spin operators is modified to exhibit peak splitting (with respect to black line reference result when $J_{sd} = 0$) at energies ϵ_0, ϵ_1, and ϵ_2. Also, few additional peaks around single-particle energy levels ϵ_0 and ϵ_2 emerge.

In Fig. 8(b), we compute $A(E)$ using truncated HP transformation with a truncation number $N_T = 6$. Although it reproduces the peak-splitting near ϵ_0, ϵ_1, and ϵ_2, it exhibits several additional peaks that are absent in the exact result in Fig. 8(a). This discrepancy can be understood as follows. The function $A(E)$ depends on the exact GS $|\Psi_0\rangle$ through Eqs. (64) and (65). However, for $N_T = 6$ Fig. 7(b) demonstrates $|\Psi_0\rangle^{\text{HP}}_{N_T=6} \neq |\Psi_0\rangle$. At first sight, it appears that the same argument should produce exact $A(E)$ in Fig. 8(c) using $N_T = 20$ because $|\Psi_0\rangle^{\text{HP}}_{N_T=20} \equiv |\Psi_0\rangle$ in Fig. 7(c). However, the discrepancy between exact $A(E)$ (red line) in Fig. 8(a) and blue line in Fig. 8(c) is explained by Eqs. (64) and (65) where $A(E)$ depends both on GS $|\Psi_0\rangle$ and excited many-body states $|\Psi_k\rangle$ [Eq. (65)] for which truncation number $N_T = 20$ appears to be *insufficient*. The repeated analysis from Figs. 8(a)–8(c) for spin-1 localized spins, but by using spin-$\frac{5}{2}$ localized spins in Figs. 8(d)–8(f), shows that requirement of large $N_T = 20$ cannot be bypassed by increasing the value of localized spins to make them more classical-like [3,60,62].

E. Magnonic spectral function in interacting system of electrons and magnons

The *exact* HP transformation in Eqs. (1) makes it possible to define magnonic spectral function $D(E)$ in Eq. (66) and compute it without any approximations by numerically evaluating square root of matrices in Eqs. (1). Using the same systems of spin-1 or spin-$\frac{5}{2}$ localized spins that are studied in Fig. 8, we first establish a reference magnonic spectral function by computing $D(E)$ in Figs. 9(a) and 9(b) with electron–localized-spin interaction turned off ($J_{sd} = 0$). Such reference $D(E)$ [Fig. 9(a)] exhibits three peaks at energies $E = 0\,\text{eV}$, $E = 0.2\,\text{eV}$, and $E = 0.6\,\text{eV}$, which correspond to available states in the presence of solely localized-spin–localized-spin (or, equivalently, magnon-magnon) interactions. Conversely, when we turn on $J_{sd} = 0.2\,\text{eV}$ in Figs. 9(c) and 9(d), we find that the original noninteracting peaks remain largely intact, except for the one near $E = 0.2\,\text{eV}$ which undergoes a tiny splitting, and far away the original peaks, $D(E)$ exhibits new additional peaks (marked by dotted circles) near energies $E = 1.6\,\text{eV}$ and $E = 2.1\,\text{eV}$. Analogous features are observed for spin-$\frac{5}{2}$ localized spins when switching from $J_{sd} = 0$ in Fig. 9(b) to $J_{sd} \neq 0$ in Fig. 9(d).

We note that similar additional peaks in magnonic spectral function, generated by turning on electron-magnon interaction, were previously observed in MBPT calculations [38] despite being based on resummation of an infinite class of selected diagrams—in contrast, calculations in Figs. 9(c) and 9(d) are nonperturbative and, therefore, correspond to all diagrams being summed to infinite order. These additional peaks in $D(E)$ computed by MBPT were interpreted in Feynman diagrammatic language as quasibound states of magnons dressed by the cloud of electron-hole pair excitations. Also, MBPT calculations of Refs. [38,92] find much smaller modification of electronic $A(E)$ upon tuning on electron-magnon interaction. This is explained by magnons being in the strongly interacting regime versus electrons being in the weakly interacting regime due to [38] J_{sd} divided by the bandwidth of noninteracting magnons being much larger than J_{sd} divided by the bandwidth of noninteracting electrons.

To clarify the origin of these peaks further in the context of our exact nonperturbative calculations in Figs. 9(c) and 9(d), we focus on the peak near $E = 1.6\,\text{eV}$ in Fig. 9(c). This peak is due to many-body excited state $|\Psi_k\rangle$ whose composition is given explicitly in Fig. 9(e). This state has a nonzero weight $Q^+_k = 0.006$ in Eq. (67). Although the value of Q^+_k appears to be small, it contributes about 2% in the sum rule in Eq. (68b) and thus it cannot be ignored. Interestingly, Fig. 9(e) reveals that this specific $|\Psi_k\rangle$ is a linear superposition of states with $N_{\text{mag}} = 0$, 1, or 2 HP bosons.

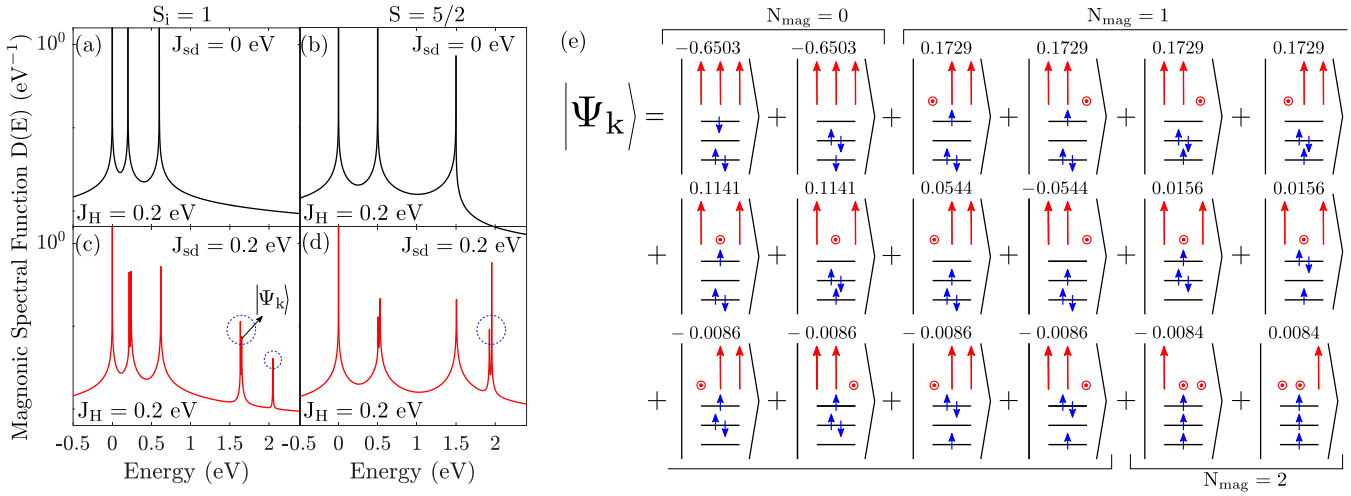

FIG. 9. (a)–(d) The *exact* magnonic spectral function $D(E)$ in Eq. (66) evaluated by mapping localized spin operators to HP bosons in a numerically exact fashion via Eqs. (1) for 1D quantum many-body system illustrated in Fig. 1(b) comprised of $N = 3$ sites hosting (a), (c) spin-1 or (b), (d) spin-$\frac{5}{2}$ localized spins. The electron–localized-spin interaction is turned off ($J_{\rm sd} = 0\,$eV) in (a) and (b) or turned on ($J_{\rm sd} = 0.2\,$eV) in (c) and (d), while keeping $J_H = 0.2\,$eV in all panels. (c), (d) Dotted circle mark additional peaks in $D(E)$ originating from excited states $|\Psi_k\rangle$, as encoded by Eq. (66). (e) Composition of specific excited quantum many-body state $|\Psi_k\rangle$ for spin-1 case which is responsible for peak in $D(E)$ near $E = 1.6\,$eV in (c)—this state is a superposition of kets with zero magnons ($N_{\rm mag} = 0$) and solely electronic excitations; followed by kets with one magnon excitation ($N_{\rm mag} = 1$); and then states with two-magnon excitations ($N_{\rm mag} = 2$). Numbers on the top of each ket are coefficients in their linear superposition leading to $|\Psi_k\rangle$.

F. Entanglement entropy of ground and excited states of interacting system of electrons and magnons

All three different versions of the GS $|\Psi_0\rangle$ in Fig. 7, as well as selected excited state $|\Psi_k\rangle$ shown in Fig. 9(e), are examples of pure but *entangled* quantum many-body states [87]. In particular, these states encode entanglement between electronic and localized-spin subsystems. The von Neumann entanglement entropy [87] for electronic or localized-spin subsystems of the total bipartite system are identical, $\mathcal{S}_e = \mathcal{S}_{\rm lspins}$, and can be computed from the reduced density matrix $\hat{\rho}_e$,

$$\mathcal{S}_e = -{\rm Tr}[\hat{\rho}_e \ln \hat{\rho}_e], \tag{73}$$

where the (improper) mixed quantum state of the electronic subsystem is described by reduced density matrix

$$\hat{\rho}_e = {\rm Tr}_{\rm lspins}|\Psi\rangle\langle\Psi|, \tag{74}$$

obtained by partial trace of the pure state density matrix, $|\Psi\rangle\langle\Psi|$, over the basis of states in $\mathcal{H}_{\rm lspins}$. For example, $\mathcal{S}_e^0 = 5.6 \times 10^{-3}$ for the exact GS in Fig. 7(a), which means that this many-body entangled state is quite close to separable (characterized by $\mathcal{S}_e \equiv 0$) noninteracting (i.e., for $J_{\rm sd} = 0$) GS as the first term depicted in Fig. 7(a). On the other hand, $\mathcal{S}_e^0 = 0.604$ for the GS in Fig. 7(b) which is incorrect [unlike the correct GS in Fig. 7(c) which matches the exact GS in Fig. 7(a)] due to too small N_T employed in truncated HP transformation (Sec. II E). Note that selected excited many-body entangled state $|\Psi_k\rangle$ analyzed in Fig. 9(e) has much larger $\mathcal{S}_e^k = 0.467$.

G. Diagonal and off-diagonal elements of time-dependent electronic and magnonic lesser Green's functions

The time-dependent electronic lesser GF $G^<_{i\sigma,j\sigma'}(t,t')$ in Eq. (59) generally depends [24,25] on two time arguments, t and t'. At equal times $t' = t$, it yields electronic one-particle *nonequilibrium* density matrix [24,55,110,111]

$$\boldsymbol{\rho}(t) = -i\hbar \mathbf{G}^<(t,t')\big|_{t'=t}. \tag{75}$$

Its diagonal elements in, e.g., coordinate (or site for discrete lattice) representation contain information about the time-dependent electronic charge and spin density [55], whereas the off-diagonal elements encode quantum-mechanical interference effects [111] and measure the degree of quantum coherence [112]. To illustrate their time evolution, we use the same 1D quantum many-body system employed in Fig. 6 where localized spin-$\frac{5}{2}$ on site $i = 1$ is completely flipped [i.e., $N_{\rm mag} = 5$ HP bosons are introduced on site $i = 1$ via Eq. (70)] to initiate nonequilibrium dynamics.

Figures 10(a)–10(d) show the ensuing time evolution for the diagonal elements, $-i\hbar G^<_{i\sigma,i\sigma}(t,t)$, as well as for the off-diagonal elements, $-i\hbar G^<_{i\sigma,j\sigma'}(t,t)$. To establish a reference result, we turn electron–localized-spin interaction off ($J_{\rm sd} = 0$) in Figs. 10(a) and 10(b), which trivially leads to all elements being time independent because for $J_{\rm sd} = 0$ the quantum state of the electronic subsystem is an eigenstate of the electronic Hamiltonian $\hat{H}_e$ [Eq. (8)].

Conversely, Figs. 10(c) and 10(d) use $J_{\rm sd} = 1\,$eV which leads to nontrivial time dependence of both diagonal and off-diagonal elements of $-i\hbar\mathbf{G}^<(t,t)$. Interestingly, the diagonal elements, $-i\hbar G^<_{i\sigma,i\sigma}(t,t)$ in Fig. 10(c) satisfy $-i\hbar[G^<_{i\uparrow,i\uparrow}(t,t) + G^<_{i\downarrow,i\downarrow}(t,t)] = Q_i$ with Q_i being the total electronic density on site i, are time independent. This means that no charge current flows between sites i and j. Instead, population of electrons with spin $\sigma = \uparrow, \downarrow$ on site i exchanges solely between spin $\sigma = \uparrow, \downarrow$ states at that site. This is also accompanied by time evolution of the off-diagonal elements $-i\hbar G^<_{i\sigma,j\sigma'}(t,t)$ in Fig. 10(d).

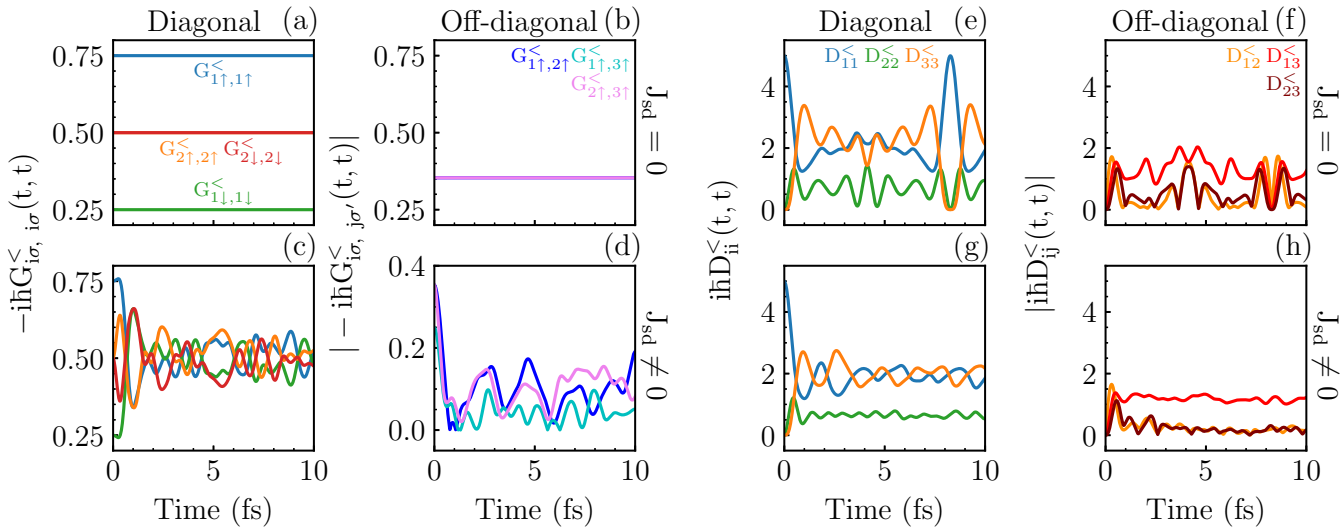

FIG. 10. Time evolution of (a) diagonal and (b) magnitude of complex off-diagonal elements of the electronic lesser GF $G^{<}_{i\sigma,j\sigma'}(t,t)$ [Eq. (59)] in the site basis for the system depicted in Fig. 1(b) composed of $N = 3$ sites hosting spin-$\frac{5}{2}$ localized spins and with electron-magnon interaction turned off ($J_{sd} = 0$). (c) and (d) are their counterparts when the electron-magnon interaction is turned on ($J_{sd} = 1$ eV). (e)–(h) show the same information as (a)–(d), but for magnonic lesser GF $D^{<}_{ij}(t,t)$ [Eq. (61)] in the site basis. Note that some of the off-diagonal elements are not explicitly shown because they are either zero or identical to the ones plotted in (b), (d) or (f), (h).

The off-diagonal elements of the lesser GF are also required to calculate many-body lesser self-energy $\mathbf{\Sigma}^{<}(t_1,t_2)$ [24,25], which is connected to a lesser GF in a self-consistent fashion via the Keldysh equation

$$\mathbf{G}^{<}(t,t') = \int_{-\infty}^{+\infty}\int_{-\infty}^{+\infty} dt_1 dt_2 \mathbf{G}^{r}(t,t_1)\mathbf{\Sigma}^{<}(t_1,t_2)\mathbf{G}^{a}(t_2,t'). \tag{76}$$

Equation (76) encapsulates time evolution of quantum many-body systems in terms of solely one-particle quantities. Here $\mathbf{G}^{a}(t,t') = [\mathbf{G}^{r}(t',t)]^{\dagger}$ is the advanced GF. A self-consistent solution to Eq. (76) can yield the exact many-body lesser self-energy. Alternatively, one can systematically approximate it [38] using the so-called conserving approximations [113] in MBPT. One such conserving approximation for the lesser self-energy of electron-boson interacting systems is the so-called self-consistent Born approximation (SCBA) [38,113–115]. The SCBA ensures charge conservation in nonequilibrium [93], and in steady-state nonequilibrium one can Fourier transform $\Sigma^{<}_{ij}(t_1 - t_2)$ to energy domain and operate with $\Sigma^{<}_{ij}(E)$.

To reduce computational complexity [114] in calculations of $\Sigma^{<}_{ij}(E)$ and enable simulations of devices containing large number of atoms, the local self-energy approximation is often employed [88–91] when modeling inelastic scattering of electrons and bosons. In this approximation, one assumes $|\Sigma^{<}_{ii}(E)| \gg |\Sigma^{<}_{ij}(E)|$, i.e., the off-diagonal elements of self-energy are minuscule when compared to the diagonal ones, and thus, one can set them to zero. This is done in conjunction with discarding the off-diagonal elements of the electronic lesser GF, i.e., $G^{<}_{ij}(E) \approx G^{<}_{ii}(E)\delta_{ij}$.

Using our numerically exact electronic lesser GF in Figs. 10(c) and 10(d), we can examine if the local self-energy approximation [88–91] is warranted for electron-magnon realization of electron-boson quantum many-body system. The off-diagonal elements of the lesser GF in Fig. 10(d) are not minuscule, but are instead approximately one-fifth of the diagonal elements in Fig. 10(c). Therefore, the local self-energy approximation in the case of many-body electron-magnon interacting systems may only be justified for a qualitative understanding and not for a quantitative one. The same general conclusion about the need to carefully handle off-diagonal elements (of self-energies and GFs) has been emphasized for a variety of many-body electron-electron systems and hosting materials [78].

Figures 10(e)–10(h) show the counterpart of Figs. 10(a)–10(d) but for the lesser GF of HP bosons. Here the off-diagonal elements of the bosonic lesser GF, $\mathbf{D}^{<}(t,t)$ in Eq. (61), at equal times (i.e., of bosonic one-particle nonequilibrium density matrix) are always comparable to the diagonal ones independently of whether the electron–localized-spin interaction J_{sd} is turned off [Figs. 10(e) and 10(f)] or turned on [Figs. 10(g) and 10(h)].

Finally, we use the exact time dependence of the off-diagonal element $D^{<}_{13}(t,t)$ of the lesser GF of HP bosons in Fig. 10(f), where $J_{sd} = 0$, and compare it to calculations employing either truncated [Fig. 11(a)] or resummed [Fig. 11(b)] HP transformation. In the former case, Fig. 11(a) shows that truncated HP transformation with $N_T = 3$ begins to deviate from the exact result on a very short timescale. On the other hand, if we use the latter with $N_{max} = 3$ [magenta solid line in Fig. 11(b)], the deviations are suppressed. Furthermore, if we choose $N_{max} = 2S = 5$, then the computed time dependence perfectly tracks the exact result [dotted green line in Fig. 11(b)]. The same conclusion remains valid when electron-magnon interaction is turned on ($J_{sd} \neq 0$) in Figs. 11(c) and 11(d) as the counterparts of Figs. 11(a) and 11(b), respectively. Akin to Fig. 6(b) computed in terms of many-body wave functions, in the presence of conduction electrons it takes longer time [Fig. 11(c)] to observe deviations between magnonic GF computed using truncated HP transformation and the same GF computed numerically exactly by evaluating the square root of bosonic operators in

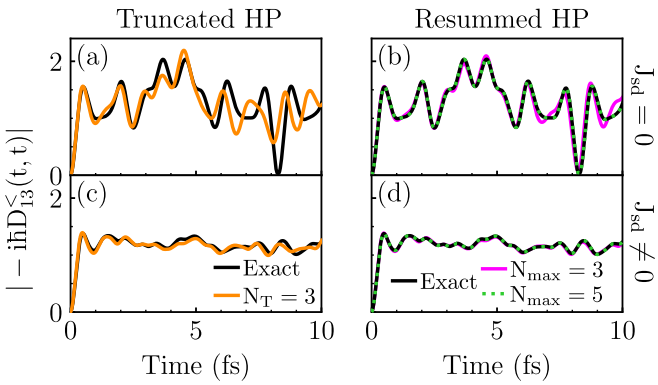

FIG. 11. Comparison of time dependence of the magnitude of the *exact* (black solid lines) off-diagonal elements of magnonic lesser GF element, $|-i\hbar D^{<}_{13}(t,t)|$, from Figs. 10(f) and 10(h) with those computed using *truncated* (orange solid lines for $N_T = 3$) and *resummed* (solid magenta and green dotted lines) HP transformation for (a), (b) electron-magnon interaction turned off ($J_{sd} = 0$) and (c), (d) electron-magnon interaction turned-on ($J_{sd} = 1$ eV).

Eqs. (1). Once ressummed HP transformation is employed, the off-diagonal elements of the magnonic GFs in the presence of conduction electrons can be obtained exactly [Fig. 11(d)] while bypassing numerical computation of the square root of bosonic operators in Eqs. (1).

IV. CONCLUSIONS

By applying numerically exact diagonalization techniques to two versions of the Hamiltonian of quantum many-body system of conduction electrons interacting with localized spins that are widely used in spintronics and magnonics, we compare predictions from these two Hamiltonians for GS and spectral functions extracted from the retarded GF in *equilibrium*; and time evolution of the expectation values of localized spin operators and lesser GF in *nonequilibrium*. The two Hamiltonians, describing systems illustrated in Fig. 1 chosen as 1D and small to make calculations tractable, differ in their treatment of localized quantum spins—they are described by either finite-size matrices of the original spin operators or infinite matrices of bosonic operators after the original localized spin operators are mapped to bosonic ones using the popular HP transformation. The truncation (Sec. II E) of HP transformation is always done to make diagrammatic MBPT [24,38] or Monte Carlo [108,109] calculations possible, but mapping of finite size to infinite matrices necessarily requires some approximations which can lead to spurious effects in equilibrium (Fig. 8) or incorrect time evolution (Figs. 4–6) out of equilibrium. Our conclusions are summarized as follows:

(1) For quantum many-body systems composed of localized spins alone, Fig. 4 shows that as more interacting HP bosons are introduced into the system, a progressively larger number of terms N_T is required in the truncated HP transformation to incorporate multimagnon interactions and accurately track the nonequilibrium dynamics of localized spins. Figure 5 shows that the breakdown time t_{break} for truncated HP transformation follows $t_{break} \propto \exp(pN_T)$. Although, the exponential dependence of t_{break} on the truncation number N_T is favorable, the reasonable value of $N_T = 1$-5 typically used in practical calculations does not allow one to track dynamics beyond ∼15 fs timescale, which is insufficient for ultrafast [102] or spin torque applications [51,53].

(2) When electrons are introduced and electron–localized-spin interaction is turned on, Figs. 6(a)–6(c) show that N_T required to accurately track nonequilibrium dynamics of localized spins is actually reduced due to the transfer of spin angular momentum between the two subsystems, which effectively reduces the total number of interacting magnons within the localized spin subsystem. Furthermore, Figs. 6(d) and 6(e) show that the recently introduced [17] resummed HP transformation (Sec. II F) makes it possible to *completely evade artifacts* of the usual truncated HP transformation. However, the electron-magnon Hamiltonian furnished by it in Eq. (72) is much more complex for MBPT and diagrammatic Monte Carlo calculations than previously used electron-magnon Hamiltonians [38] based on low-order truncated HP transformation.

(3) Figure 7 reveals how truncated HP transformation with a small truncation number [such as $N_T = 6$ in Fig. 7(b)] produces an incorrect GS of the interacting electron-magnon system. Only when truncation number is increased [such as to $N_T = 20$ in Fig. 7(c)], exact diagonalization of electron-boson Hamiltonian reproduces the exact GS obtained by diagonalizing the original electron–localized-spin-operators Hamiltonian [Fig. 7(a)]. However, even a large truncation number [such as $N_T = 20$ in Figs. 8(c) and 8(f)] does not ensure that correct electronic spectral function can be obtained from electron-boson Hamiltonian due to the fact that spectral functions depend [Eq. (64)] on *both* the GS and excited quantum many-body states.

(4) The magnonic spectral function can be substantially modified [Figs. 9(c) and 9(d)] upon introduction of conduction electrons and their interaction with localized spins, even when such interaction appears small for electrons, due to much smaller bandwidth of magnons. That is, magnons are effectively pushed into strongly interacting regime, and the new peaks in their spectral function (or interacting density of states [85,86]) can be directly related to specific excited quantum many-body states. The structure of excited states [Fig. 9(a)] reveals superpositions of many-body states in which holes in electronic single particle levels are formed and accompanied by flips of localized spins or, equivalently, creation of one or more virtual HP bosons.

(5) The time evolution of the matrix elements of the lesser GF (electronic or magnonic) at equal times in real-space representation, which yields the one-particle nonequilibrium density matrix in real-space representation, shows that the magnitude of the off-diagonal elements is always comparable to the magnitude of the diagonal ones (Fig. 10). Thus, the local self-energy approximation neglecting the off-diagonal elements, as often employed [88–91] to enable MBPT modeling of electron-boson systems with a large number of atoms, is not warranted. Lastly, by using the exact time time evolution of an off-diagonal magnonic lesser GF element, in Fig. 11, we show that these off-diagonal elements can be accurately described by the resummed HP transformation but not by the truncated HP transformation.

ACKNOWLEDGMENTS

This research was primarily supported by the U.S. National Science Foundation (NSF) through the University of Delaware Materials Research Science and Engineering Center DMR-2011824. The paper originated from Research Projects Based Learning implemented within a graduate course PHYS814: Advanced Quantum Mechanics [116] at the University of Delaware.

[1] F. Bloch, Zur Theorie des Ferromagnetismus, Z. Phys. **61**, 206 (1930).

[2] A. V. Chumak, V. I. Vasyuchka, A. A. Serga, and B. Hillebrands, Magnon spintronics, Nat. Phys. **11**, 453 (2015).

[3] R. Wieser, Description of a dissipative quantum spin dynamics with a Landau-Lifshitz-Gilbert like damping and complete derivation of the classical Landau-Lifshitz equation, Euro. Phys. J. B **88**, 77 (2015).

[4] S.-K. Kim, Micromagnetic computer simulations of spin waves in nanometre-scale patterned magnetic elements, J. Phys. D: Appl. Phys. **43**, 264004 (2010).

[5] R. F. L. Evans, W. J. Fan, P. Chureemart, T. A. Ostler, M. O. A. Ellis, and R. W. Chantrell, Atomistic spin model simulations of magnetic nanomaterials, J. Phys.: Condens. Matter **26**, 103202 (2014).

[6] M. E. Zhitomirsky and A. L. Chernyshev, *Colloquium*: Spontaneous magnon decays, Rev. Mod. Phys. **85**, 219 (2013).

[7] T. Holstein and H. Primakoff, Field dependence of the intrinsic domain magnetization of a ferromagnet, Phys. Rev. **58**, 1098 (1940).

[8] G. D. Mahan, *Condensed Matter in a Nutshell* (Princeton University Press, Princeton, 2011).

[9] E. M. Chudnovsky and J. Tejada, *Lectures on Magnetism* (Rinton Press, Paramus, 2006).

[10] S.-K. Kim, H. Ochoa, R. Zarzuela, and Y. Tserkovnyak, Realization of the Haldane-Kane-Mele Model in a System of Localized Spins, Phys. Rev. Lett. **117**, 227201 (2016).

[11] A. Mook, K. Plekhanov, J. Klinovaja, and D. Loss, Interaction-Stabilized Topological Magnon Insulator in Ferromagnets, Phys. Rev. X **11**, 021061 (2021).

[12] M. Elyasi, Y. M. Blanter, and G. E. W. Bauer, Resources of nonlinear cavity magnonics for quantum information, Phys. Rev. B **101**, 054402 (2020).

[13] I. S. Tupitsyn, P. C. E. Stamp, and A. L. Burin, Stability of Bose-Einstein Condensates of Hot Magnons in Yttrium Iron Garnet Films, Phys. Rev. Lett. **100**, 257202 (2008).

[14] H. Y. Yuan and R. A. Duine, Magnon antibunching in a nanomagnet, Phys. Rev. B **102**, 100402(R) (2020).

[15] S. Takei, Spin transport in an electrically driven magnon gas near Bose-Einstein condensation: Hartree-Fock-Keldysh theory, Phys. Rev. B **100**, 134440 (2019).

[16] S. M. Radošević, Magnon-magnon interactions in $O(3)$ ferromagnets and equations of motion for spin operators, Ann. Phys. **362**, 336 (2015).

[17] M. Vogl, P. Laurell, H. Zhang, S. Okamoto, and G. A. Fiete, Resummation of the Holstein-Primakoff expansion and differential equation approach to operator square roots, Phys. Rev. Res. **2**, 043243 (2020).

[18] J. König and A. Hucht, Newton series expansion of bosonic operator functions, SciPost Phys. **10**, 007 (2021).

[19] F. J. Dyson, General theory of spin-wave interactions, Phys. Rev. **102**, 1217 (1956).

[20] C. P. Hofmann, Spontaneous magnetization of an ideal ferromagnet: Beyond Dyson's analysis, Phys. Rev. B **84**, 064414 (2011).

[21] A. Schuckert, A. Piñeiro Orioli, and J. Berges, Nonequilibrium quantum spin dynamics from two-particle irreducible functional integral techniques in the Schwinger boson representation, Phys. Rev. B **98**, 224304 (2018).

[22] C. Broholm, R. J. Cava, S. A. Kivelson, D. G. Nocera, M. R. Norman, and T. Senthil, Quantum spin liquids, Science **367**, 263 (2020).

[23] Z. Zhuang and J. B. Marston, Spin transport in a quantum spin orbital liquid, Phys. Rev. B **104**, L060403 (2021).

[24] G. Stefanucci and R. van Leeuwen, *Nonequilibrium Many-Body Theory of Quantum Systems: A Modern Introduction* (Cambridge University Press, Cambridge, 2013).

[25] N. Schlünzen, S. Hermanns, M. Scharnke, and M. Bonitz, Ultrafast dynamics of strongly correlated fermions-nonequilibrium Green functions and self-energy approximations, J. Phys.: Condens. Matter **32**, 103001 (2020).

[26] R. van Leeuwen and G. Stefanucci, Wick theorem for general initial states, Phys. Rev. B **85**, 115119 (2012).

[27] R. Kubo, The spin-wave theory as a variational method and its application to antiferromagnetism, Rev. Mod. Phys. **25**, 344 (1953).

[28] A. B. Harris, D. Kumar, B. I. Halperin, and P. C. Hohenberg, Dynamics of an antiferromagnet at low temperatures: Spin-wave damping and hydrodynamics, Phys. Rev. B **3**, 961 (1971).

[29] C. J. Hamer, Z. Weihong, P. Arndt, Third-order spin-wave theory for the Heisenberg antiferromagnet, Phys. Rev. B **46**, 6276 (1992).

[30] S. V. Maleev, Scattering of slow neutrons in ferromagnets, Sov. Phys. JETP **6**, 776 (1958).

[31] P. Jordan and E. Wigner, Über das Paulische Äquivalenzverbot, Z. Phys. **47**, 631 (1928).

[32] I. Affleck and J. B. Marston, Large-n limit of the Heisenberg-Hubbard model: Implications for high-T_c superconductors, Phys. Rev. B **37**, 3774(R) (1988).

[33] A. M. Tsvelik, New Fermionic Description of Quantum Spin Liquid State, Phys. Rev. Lett. **69**, 2142 (1992).

[34] P. Coleman, C. Pépin, and A. M. Tsvelik, Phys. Rev. B **62**, 3852 (2000).

[35] M. N. Kiselev and R. Oppermann, Schwinger-Keldysh Semionic Approach for Quantum Spin Systems, Phys. Rev. Lett. **85**, 5631 (2000).

[36] M. Marcuzzi, J. Marino, A. Gambassi, and A. Silva, Prethermalization from a low-density Holstein-Primakoff expansion, Phys. Rev. B **94**, 214304 (2016).

[37] J. G. Hirsch, O. Castaños, R. López-Peña, and E. Nahmad-Achar, Virtues and limitations of the truncated Holstein-Primakoff description of quantum rotors, Phys. Scr. **87**, 038106 (2013).

[38] F. Mahfouzi and B. K. Nikolić, Signatures of electron-magnon interaction in charge and spin currents through magnetic tunnel junctions: A nonequilibrium many-body perturbation theory approach, Phys. Rev. B **90**, 045115 (2014).

[39] T. Tay and L. J. Sham, Theory of atomistic simulation of spin-transfer torque in nanomagnets, Phys. Rev. B **87**, 174407 (2013).

[40] Y. Cheng, W. Wang, and S. Zhang, Amplification of spin-transfer torque in magnetic tunnel junctions with an antiferromagnetic barrier, Phys. Rev. B **99**, 104417 (2019).

[41] S. A. Bender, R. A. Duine, and Y. Tserkovnyak, Quantum spin-transfer torque and magnon-assisted transport in nanostructures, Phys. Rev. B **99**, 024434 (2019).

[42] P. Tang, X. Han, and S. Zhang, Quantum theory of spin-torque driven magnetization switching, Phys. Rev. B **103**, 094442 (2021).

[43] N. Okuma and K. Nomura, Microscopic derivation of magnon spin current in a topological insulator/ferromagnet heterostructure, Phys. Rev. B **95**, 115403 (2017).

[44] E. G. Tveten, A. Brataas, and Y. Tserkovnyak, Electron-magnon scattering in magnetic heterostructures far out of equilibrium, Phys. Rev. B **92**, 180412(R) (2015).

[45] J. Zheng, S. Bender, J. Armaitis, R. E. Troncoso, and R. A. Duine, Green's function formalism for spin transport in metal-insulator-metal heterostructures, Phys. Rev. B **96**, 174422 (2017).

[46] R. E. Troncoso, A. Brataas, and R. A. Duine, Many-body theory of spin-current driven instabilities in magnetic insulators, Phys. Rev. B **99**, 104426 (2019).

[47] H. Adachi, J.-I. Ohe, S. Takahashi, and S. Maekawa, Linear-response theory of spin Seebeck effect in ferromagnetic insulators, Phys. Rev. B **83**, 094410 (2011).

[48] A. Kamra and W. Belzig, Super-Poissonian Shot Noise of Squeezed-Magnon Mediated Spin Transport, Phys. Rev. Lett. **116**, 146601 (2016).

[49] T. S. Parvini, V. A. S. V. Bittencourt, and S. V. Kusminskiy, Antiferromagnetic cavity optomagnonics, Phys. Rev. Res. **2**, 022027(R) (2020).

[50] S. A. Bender, A. Kamra, W. Belzig, and R. A. Duine, Spin Current Cross-Correlations as a Probe of Magnon Coherence, Phys. Rev. Lett. **122**, 187701 (2019).

[51] D. Ralph and M. Stiles, Spin transfer torques, J. Magn. Magn. Mater. **320**, 1190 (2008).

[52] M. D. Petrović, P. Mondal, A. Feiguin, P. P. Plecháč, and B. K. Nikolić, Spintronics Meets Density Matrix Renormalization Group: Quantum Spin-Torque-Driven Nonclassical Magnetization Reversal and Dynamical Buildup of Long-Range Entanglement, Phys. Rev. X **11**, 021062 (2021).

[53] D. V. Berkov and J. Miltat, Spin-torque driven magnetization dynamics: Micromagnetic modeling, J. Magn. Magn. Mater. **320**, 1238 (2008).

[54] M. O. A. Ellis, M. Stamenova, and S. Sanvito, Multiscale modeling of current-induced switching in magnetic tunnel junctions using *ab initio* spin-transfer torques, Phys. Rev. B **96**, 224410 (2017).

[55] M. D. Petrović, B. S. Popescu, U. Bajpai, P. Plecháč, and B. K. Nikolić, Spin and Charge Pumping by a Steady or Pulse-Current-Driven Magnetic Domain Wall: A Self-Consistent Multiscale Time-Dependent Quantum-Classical Hybrid Approach, Phys. Rev. Appl. **10**, 054038 (2018).

[56] U. Bajpai and B. K. Nikolić, Time-retarded damping and magnetic inertia in the Landau-Lifshitz-Gilbert equation self-consistently coupled to electronic-time-dependent nonequilibrium Green functions, Phys. Rev. B **99**, 134409 (2019).

[57] A. Suresh, U. Bajpai, and B. K. Nikolić, Magnon-driven chiral charge and spin pumping and electron-magnon scattering from time-dependent quantum transport combined with classical atomistic spin dynamics, Phys. Rev. B **101**, 214412 (2020).

[58] A. Suresh, U. Bajpai, M. D. Petrović, H. Yang, and B. K. Nikolić, Magnon- versus Electron-Mediated Spin-Transfer Torque Exerted by Spin Current Across an Antiferromagnetic Insulator to Switch the Magnetization of an Adjacent Ferromagnetic Metal, Phys. Rev. Appl. **15**, 034089 (2021).

[59] U. Bajpai and B. K. Nikolić, Spintronics Meets Nonadiabatic Molecular Dynamics: Geometric Spin Torque and Damping on Dynamical Classical Magnetic Texture Due to an Electronic Open Quantum System, Phys. Rev. Lett. **125**, 187202 (2020).

[60] C. Stahl and M. Potthoff, Anomalous Spin Precession Under a Geometrical Torque, Phys. Rev. Lett. **119**, 227203 (2017).

[61] E. V. Boström and C. Verdozzi, Steering magnetic skyrmions with currents: A nonequilibrium Green's functions approach, Phys. Stat. Solidi B **256**, 1800590 (2019).

[62] J. P. Gauyacq and N. Lorente, Classical limit of a quantal nano-magnet in an anisotropic environment, Surf. Sci. **630**, 325 (2014).

[63] P. Mondal, A. Suresh, and B. K. Nikolić, When can localized spins interacting with conduction electrons in ferro- or antiferromagnets be described classically via the Landau-Lifshitz equation: Transition from quantum many-body entangled to quantum-classical nonequilibrium states, arXiv:2107.10776 [Phys. Rev. B (to be published)].

[64] P. Mondal, U. Bajpai, M. D. Petrović, P. P. Plecháč, and B. K. Nikolić, Quantum spin-transfer torque induced nonclassical magnetization dynamics and electron-magnetization entanglement, Phys. Rev. B **99**, 094431 (2019).

[65] M. D. Petrović, P. Mondal, A. E. Feiguin, and B. K. Nikolić, Quantum Spin Torque Driven Transmutation of an Antiferromagnetic Mott Insulator, Phys. Rev. Lett. **126**, 197202 (2021).

[66] A. Mitrofanov and S. Urazhdin, Energy and momentum conservation in spin transfer, Phys. Rev. B **102**, 184402 (2020).

[67] A. Mitrofanov and S. Urazhdin, Nonclassical Spin Transfer Effects in an Antiferromagnet, Phys. Rev. Lett. **126**, 037203 (2021).

[68] A. Zholud, R. Freeman, R. Cao, A. Srivastava, and S. Urazhdin, Spin Transfer Due to Quantum Magnetization Fluctuations, Phys. Rev. Lett. **119**, 257201 (2017).

[69] Y. Wang, J. P. Dehollain, F. Liu, U. Mukhopadhyay, M. S. Rudner, L. M. K. Vandersypen, and E. Demler, *Ab initio* exact diagonalization simulation of the Nagaoka transition in quantum dots, Phys. Rev. B **100**, 155133 (2019).

[70] J. B. Parkinson, J. C. Bonner, G. Müller, M. P. Nightingale, and H. W. J. Blöte, Heisenberg spin chains: Quantum-classical crossover and the Haldane conjecture, J. Appl. Phys. **57**, 3319 (1985).

[71] R. L. Cooper and E. A. Uehling, Ferromagnetic resonance and spin diffusion in supermalloy, Phys. Rev. **164**, 662 (1967).

[72] A. M. Tsvelik and O. M. Yevtushenko, Chiral Spin Order in Kondo-Heisenberg Systems, Phys. Rev. Lett. **119**, 247203 (2017).

[73] A. Spinelli, B. Bryant, F. Delgado, J. Fernández-Rossier, and A. F. Otte, Imaging of spin waves in atomically designed nanomagnets, Nat. Mater. **13**, 782 (2014).

[74] S. Loth, S. Baumann, C. P. Lutz, D. M. Eigler, and A. J. Heinrich, Bistability in atomic-scale antiferromagnets, Science **335**, 196 (2012).

[75] R. Schumann and D. Zwicker, The Hubbard model extended by nearest-neighbor Coulomb and exchange interaction on a cubic cluster—rigorous and exact results, Ann. Phys. (Berlin) **522**, 419 (2010).

[76] D. J. Carrascal, J. Ferrer, J. C. Smith, and K. Burke, The Hubbard dimer: A density functional case study of a many-body problem, J. Phys.: Condens. Matter **27**, 393001 (2015).

[77] S. Hermanns, N. Schlünzen, and M. Bonitz, Hubbard nanoclusters far from equilibrium, Phys. Rev. B **90**, 125111 (2014).

[78] J. Fei, C.-N. Yeh, D. Zgid, and E. Gull, Analytical continuation of matrix-valued functions: Carathéodory formalism, Phys. Rev. B **104**, 165111 (2021).

[79] N. Säkkinen, Y. Peng, H. Appel, and R. van Leeuwen, Many-body Green's function theory for electron-phonon interactions: Ground state properties of the Holstein dimer, J. Chem. Phys. **143**, 234101 (2015).

[80] N. Säkkinen, Y. Peng, H. Appel, and Robert van Leeuwen, Many-body Green's function theory for electron-phonon interactions: The Kadanoff-Baym approach to spectral properties of the Holstein dimer, J. Chem. Phys. **143**, 234102 (2015).

[81] T. Dimitrov, J. Flick, M. Ruggenthaler and A. Rubio, Exact functionals for correlated electron-photon systems, New J. Phys. **19**, 113036 (2017).

[82] I. Esterlis, B. Nosarzewski, E. W. Huang, B. Moritz, T. P. Devereaux, D. J. Scalapino, and S. A. Kivelson, Breakdown of the Migdal-Eliashberg theory: A determinant quantum Monte Carlo study, Phys. Rev. B **97**, 140501(R) (2018).

[83] J. Gukelberger, L. Huang, and P. Werner, On the dangers of partial diagrammatic summations: Benchmarks for the two-dimensional Hubbard model in the weak-coupling regime, Phys. Rev. B **91**, 235114 (2015).

[84] E. Kozik, M. Ferrero, and A. Georges, Nonexistence of the Luttinger-Ward Functional and Misleading Convergence of Skeleton Diagrammatic Series for Hubbard-Like Models, Phys. Rev. Lett. **114**, 156402 (2015).

[85] M. Balzer, N. Gdaniec, and M. Potthoff, Krylov-space approach to the equilibrium and nonequilibrium single-particle Green's function, J. Phys.: Condens. Matter **24**, 035603 (2011).

[86] A. Nocera, F. H. L. Essler, and A. E. Feiguin, Finite-temperature dynamics of the Mott insulating Hubbard chain, Phys. Rev. B **97**, 045146 (2018).

[87] G. De Chiara and A. Sanpera, Genuine quantum correlations in quantum many-body systems: A review of recent progress, Rep. Prog. Phys. **81**, 074002 (2018).

[88] M. Luiser and G. Kilmeck, Atomistic full-band simulations of silicon nanowire transistors: Effects of electron-phonon coupling, Phys. Rev. B **80**, 155430 (2009).

[89] R. Rhyner and M. Luiser, Atomistic modeling of coupled electron-phonon transport in nanowire transistors, Phys. Rev. B **89**, 235311 (2014).

[90] N. Cavassilas, F. Michelini, and M. Bescond, On the local approximation of the electron-photon self-energy, J. Comput. Electron. **15**, 1233 (2016).

[91] M. Moussavou, M. Lannoo, N. Cavassilas, D. Logoteta, and M. Bescond, Physically based Diagonal Treatment of the Self-Energy of Polar Optical Phonons: Performance Assessment Of III-V Double-Gate Transistors, Phys. Rev. Appl. **10**, 064023 (2018).

[92] R. B. Woolsey and R. M. White, Electron-magnon interaction in Ferromagnetic semiconductors, Phys. Rev. B **1**, 4474 (1970).

[93] T. Frederiksen, Inelastic electron transport in nanosystems, M. S. thesis, Technical University of Denmark, 2004.

[94] J-M. Reiner, M. Marthaler, J. Braumüller, M. Weides, and G. Schön, Emulating the one-dimensional Fermi-Hubbard model by a double chain of qubits, Phys. Rev. A **94**, 032338 (2016).

[95] C. Cade, L. Mineh, A. Montanaro, and S. Stanisic, Strategies for solving the Fermi-Hubbard model on near-term quantum computers, Phys. Rev. B **102**, 235122 (2020).

[96] D. Wells and H. Quiney, A fast and adaptable method for high accuracy integration of the time-dependent Schrödinger equation, Sci. Rep. **9**, 782 (2019).

[97] D. Lachance-Quirion, S. P. Wolski, Y. Tabuchi, S. Kono, K. Usami, and Y. Nakamura, Entanglement-based single-shot detection of a single magnon with a superconducting qubit, Science **367**, 425 (2020).

[98] T. Fukuhara, P. Schauß, M. Endres, S. Hild, M. Cheneau, I. Bloch, and C. Gross, Microscopic observation of magnon bound states and their dynamics, Nature (London) **502**, 76 (2013).

[99] M. Haque, Self-similar spectral structures and edge-locking hierarchy in open-boundary spin chains, Phys. Rev. A **82**, 012108 (2010).

[100] T. Morimae, A. Sugita, and A. Shimizu, Macroscopic entanglement of many-magnon states, Phys. Rev. A **71**, 032317 (2005).

[101] A. Marini and Y. Pavlyukh, Functional approach to the electronic and bosonic dynamics of many-body systems perturbed with an arbitrary strong electron-boson interaction, Phys. Rev. B **98**, 075105 (2018).

[102] F. Siegrist, J. A. Gessner, M. Ossiander, C. Denker, Yi-P. Chang, M. C. Schröder, A. Guggenmos, Y. Cui, J. Walowski, U. Martens *et al.*, Light-wave dynamic control of magnetism, Nature (London) **571**, 240 (2019).

[103] S. R. White and A. E. Feiguin, Real-Time Evolution using the Density Matrix Renormalization Group, Phys. Rev. Lett. **93**, 076401 (2004).

[104] P. Schmitteckert, Nonequilibrium electron transport using the density matrix renormalization group method, Phys. Rev. B **70**, 121302(R) (2004).

[105] A. J. Daley, C. Kollath, U. Schollwöck, and G. Vidal, Time-dependent density-matrix renormalization-group using adaptive effective Hilbert spaces, J. Stat. Mech: Theor. Exp. (2004) P04005.

[106] A. E. Feiguin, The density matrix renormalization group and its time-dependent variants, AIP Conf. Proc. **1419**, 5 (2011).

[107] E. M. Stoudenmire and S. R. White, Studying two-dimensional systems with the density matrix renormalization group, Annu. Rev. Condens. Matter Phys. **3**, 111 (2012).

[108] C. Bertrand, O. Parcollet, A. Maillard, and X. Waintal, Quantum Monte Carlo algorithm for out-of-equilibrium Green's functions at long times, Phys. Rev. B **100**, 125129 (2019).

[109] C. Bertrand, S. Florens, O. Parcollet, and X. Waintal, Reconstructing Nonequilibrium Regimes of Quantum Many-Body Systems from the Analytical Structure of Perturbative Expansions, Phys. Rev. X **9**, 041008 (2019).

[110] B. Gaury, J. Weston, M. Santin, M. Houzet, C. Groth, and X. Waintal, Numerical simulations of time-resolved quantum electronics, Phys. Rep. **534**, 1 (2014).

[111] U. Bajpai, B. S. Popescu, P. P. Plecháč, B. K. Nikolić, L. E. F. F. Torres, H. Ishizuka, and N. Nagaosa, Spatio-temporal dynamics of shift-current quantum pumping by femtosecond light pulse, J. Phys. Mater. **2**, 025004 (2019).

[112] M. Schlosshauer, Decoherence, measurement problem, and the interpretations of quantum mechanics, Rev. Mod. Phys. **76**, 1267 (2005).

[113] H. Mera, T. G. Pedersen, and B. K. Nikolić, Hypergeometric resummation of self-consistent sunset diagrams for electron-boson quantum many-body systems out of equilibrium, Phys. Rev. B **94**, 165429 (2016).

[114] T. Frederiksen, M. Paulsson, M. Brandbyge, and A.-P. Jauho, Inelastic transport theory from first principles: Methodology and application to nanoscale devices, Phys. Rev. B **75**, 205413 (2007).

[115] W. Lee, N. Jean, and S. Sanvito, Exploring the limits of the self-consistent Born approximation for inelastic electronic transport, Phys. Rev. B **79**, 085120 (2009).

[116] PHYS814: Advanced Quantum Mechanics, https://wiki.physics.udel.edu/phys814/.